Acta Materialia 220 (2021) 117333

Contents lists available at ScienceDirect

Acta Materialia

journal homepage: www.elsevier.com/locate/actamat

Full Length Article

In situ characterization of the functional degradation of a [00$\bar{1}$] orientated Fe–Mn–Al–Ni single crystal under compression using acoustic emission measurements

Anja Weidner[a,*], Alexei Vinogradov[b], Malte Vollmer[c], Phillip Krooß[c], Mario J. Kriegel[d], Volker Klemm[d], Yuri Chumlyakov[e], Thomas Niendorf[c], Horst Biermann[a]

[a] Institute of Materials Engineering, Technische Universität Bergakademie Freiberg, Freiberg, Germany
[b] Department of Mechanical and Industrial Engineering, Norwegian University of Science and Technology-NTNU, Trondheim, Norway
[c] Institute of Materials Engineering, University of Kassel, Kassel, Germany
[d] Institute of Materials Science, Technische Universität Bergakademie Freiberg, Freiberg, Germany
[e] Siberian Physical Technical Institute, State University Tomsk, Russia

ARTICLE INFO

Article history:
Received 5 May 2021
Revised 30 August 2021
Accepted 15 September 2021
Available online 19 September 2021

Keywords:
Iron-based shape memory alloy
Acoustic emission
Martensitic phase transformation
Superelasticity

ABSTRACT

Acoustic emission (AE) measurements were conducted *in situ* during cyclic compressive loading on an [00$\bar{1}$] orientated single crystal of Fe-Mn-Al-Ni shape memory alloy to study functional degradation of its superelastic response. The acoustic investigations were corroborated by optical microscopy, employing video imaging, and transmission electron microscopy. The analysis of acoustic emissions recorded during repeated loading and unloading sessions revealed two categories of AE signals that are differed by their characteristics in time and frequency domains. These two distinct types of AE signals were related to two underlying mechanisms: (i) the nucleation and reverse transformation of stress-induced (twinned) martensite, and (ii) the lateral growth and shrinkage of one dominant martensite variant and related dislocation activities, respectively. In addition, an asymmetry in the AE activity during forward and reverse transformation during mechanical loading and unloading was detected. In particular, an unexpected high AE activity was observed during the superelastic unloading of martensitic microstructure from the point of maximum load/strain. This effect was attributed to the reverse transformation of small, tiny areas of martensite as well as to unpinning and annihilation effects related to dislocations.

1. Introduction

The superelastic behavior (also commonly referred to as "pseudoelasticity") of shape memory alloys (SMAs) sets in at a critical stress when elastically loaded austenite undergoes the phase transformation into martensite [1]. Unloading initiates the reverse transformation of the metastable martensitic phase because only austenite is stable in the stress-free state at a given temperature above the austenite finish temperature A_f. The critical transformation stress on unloading is lower than that on the loading path, causing energy dissipation associated with a hysteretic stress-strain response commonly known as the superelastic effect.

Ni-Ti-based shape memory alloys are among the commercially most successful SMA systems exhibiting superelasticity [2,3]. Since their invention in the early 60s, plenty of applications have benefited from the superelastic behavior of these materials; these include, for example, medical devices or actuators [2,4]. However, high processing and material costs still prevent the wider adoption of Ni-Ti-based alloys, in particular, in material-intensive applications [4,5]. Therefore, the development of cost-efficient alternatives to Ni-Ti is among the challenges to be addressed to broaden the application range of SMAs. To this end, iron-based SMAs are considered promising [6–15]. Specifically, these materials are thought to be used for joining elements or damping applications in civil engineering. Besides the lower costs, the advantage of these alloy systems is the comparatively simple processing route bearing its origin from the steel industry [16]. Up to now, two different alloy systems have been developed showing large superelastic transformation strains at room temperature: (i) Fe-Ni-Co-Al based SMAs proposed by Tanaka et al. [17] in 2010, and (ii) Fe-Mn-Al-Ni based SMAs introduced by Omori et al. [18] in 2011. Both alloy systems exhibit a disordered parent phase with ordered, coherent precipitates having a size of a few nanometres. The precipitation of such phases is crucial to observe thermoelastic martensitic transformations [19,20] in iron-based SMAs. Such precipitates strengthen the

* Corresponding author.
E-mail address: weidner@ww.tu-freiberg.de (A. Weidner).

https://doi.org/10.1016/j.actamat.2021.117333

matrix via the formation of coherent stress fields, impede dislocation slip and reduce the temperature hysteresis by several hundred Kelvin [9,20–22]. Moreover, the size and the volume fraction of precipitates exert a strong influence on the transformation temperatures and the superelastic behavior by affecting the chemical and non-chemical contribution of the free Gibbs energy [23–27]. The significant role played by precipitates was also observed in functional fatigue experiments revealing a strong interaction between the martensitic phase and precipitates [28,29]. The understanding of functional fatigue and its mechanisms is essential for potential industrial applications. Recently, an unusual degradation mechanism in Fe-Mn-Al-Ni was reported by some of the authors of the present study [28,30]. It was shown that the phase transformation in formerly transformed areas was strongly inhibited. Instead, new previously untransformed areas were activated in the subsequent cycles. The *post mortem* TEM studies revealed that (i) the lattice misfit between the parent bcc α-phase and the martensitic fcc γ'-phase, (ii) the interaction of martensite variants, and (iii) the interaction between martensite and β precipitates are the key factors responsible for the pronounced functional degradation. However, it is still unclear in which specific order the contributing elementary mechanisms dominate the transformation pathway in the course of the superelastic cycle.

The martensitic transformation is a first-order diffusionless, displacive solid-state phase transition. It occurs with notable local stress relaxation by rapid coordinated lattice deformation giving rise to detectable acoustic emission (AE) [31]. The AE method, therefore, has long been recognized as a tool of choice for continuous *in situ* monitoring and investigation of the evolution of microstructure occurring during martensitic transformations. Using the elastodynamic approach and considering the smallest displacements detectable by an AE transducer being of the order of 10^{-14} m, Simmons and Wadley [31] have estimated the minimum detectable volume of the transformed martensite to be as small as 1 μm^3. According to their mechanistic modeling approach based on Green's function formalism, the AE signal amplitude at the sensor output appears to be proportional to the transformed volume in a homogeneous elastic media. In fair agreement with this prediction, Kannatey-Asibu and Pingsha [32] has shown that the total AE root mean square is directly proportional to the mass or volume transformed.

The use of the AE technique allows for discriminating between different transformation stages [33] and/or different forms of martensite [34]. Thus, the plethora of experimental results [35,36] backed by theoretical considerations [31] indicates that a close relationship exists between the transformation kinetics and AE. Furthermore, the activation of different mechanisms of stress relaxation during loading or thermal cycles can be potentially accounted for by the advanced statistical analysis of AE time series [37–39]. Using the AE technique paired with microscopic optical observations [33,40], two stages can be discerned with regard to the behavior of the martensitic phase: (i) the rapid nucleation and longitudinal growth of thin martensite plates (Stage I) followed by (ii) the subsequent thickening of the martensite plate by the transverse movement of the interfaces (Stage II). After nucleation, the martensite grows very fast at a sizable fraction of the velocity of sound. Nishiyama [41] has classified the rate of martensitic growth into three different velocity regimes. The quickest process is associated with athermal martensitic transformations, which occurs at approximately 10^3 m/s. However, this estimation is very crude. Using a combination of magnetic measurements and the frequency-dependent media attenuation in the AE measurements, Yu and Clapp have obtained that the martensite growth velocity consistently ranges from 0.25 to 0.65 of the shear wave velocity in the material [42] (see also references therein). This is by far higher than the estimation by Takashima et al. [43], who found the transformation propagation velocity to be of 160–200 m/s in metastable 304 stainless steel according to the analysis of AE frequency spectra. Lateral growth (thickening) of the martensitic phase occurs at substantially lower average velocity, resembling the evolution of twins in hcp metals [39].

The aim of the present paper is to unveil the kinetics of martensitic transformation and degradation of the superelastic effect in the Fe-Mn-Al-Ni iron-based shape memory alloy. For this purpose, isothermal (room temperature) cyclic compression tests were conducted on the [00$\bar{1}$]-orientated Fe–Mn–Al–Ni single crystal. The mechanical test was instrumented with the *in situ* AE measuring system and direct optical microscopic (OM) video recorder. The results of *in situ* observations were corroborated by *post mortem* transmission electron microscopy (TEM) investigations.

2. Materials and methods

2.1. Specimen preparation and mechanical testing

A single crystal of Fe–34.8 Mn–13.5 Al–7.4 Ni (at.-%) SMA was grown by the Bridgman technique, and the specimens with 3 × 3 × 6 mm^3 dimensions were wire-cut by electro-discharging. The specimens were ground to 5 µm grit size, sealed into fused silica under argon atmosphere and homogenized at 1200 °C for 20 h. Subsequent quenching was carried out in warm water at 70 °C. Ageing at 200 °C for 3 h was performed to adjust nanometre-sized β B2-type precipitates enriched by Al and Ni and avoid room temperature ageing of the microstructure. The size of these precipitates was about 10 nm (see [30,44] for details). For further testing, the specimens were again ground to 5 µm grit size and vibration-polished to a mirror-like finish.

The crystallographic orientation of the loading axis of the single crystal was double-checked by the electron backscattered diffraction (EBSD) technique using a field-emission scanning electron microscope (Mira 3 XMU, Tescan, Brno, Czech Republic) equipped with the EDAX/TSL detector and software. Based on this analysis, the loading axis was close to [00$\bar{1}$] and the surface plane normal directions corresponded to [$\bar{1}\bar{1}$0] and [1$\bar{1}$0].

The specimen was mounted between two parallel tungsten-carbide platens in a rigid 10 kN testing module (Kammrath and Weiss, Dortmund, Germany). The cyclic loading was performed along the [00$\bar{1}$] direction in a zero-compression mode to 25 cycles with a constant crosshead velocity of 5 µm/s. The loading was conducted up to a nominal total strain value of 7.5% per cycle.

During testing, the surface was continuously monitored by an optical microscope (Nikon Eclipse ME 600) equipped with a digital camera (Leica DFC 280), allowing for imaging with 1280 × 1024 pixels resolution at the frame rate of 100 s^{-1}.

A piezoelectric AE sensor Pico (Mistras, USA) with a frequency band of 300–1000 kHz was attached with a rubber band to one of the platens in close proximity to the specimen. Vacuum oil was used as coupling media. The AE signals were amplified by 60 dB by a low-noise pre-amplifier 2/4/6 and acquired by a 16-bit PCI-2 board (Mistras, USA) operated in a continuous mode at the sampling rate of 2 Msamples/s.

The microstructure of the tested specimen was investigated after the 25th cycle using transmission electron microscopy on TEM lamellae prepared by focused ion beam milling and taken by the lift-out technique (Helios Nanolab 600i, FEI, USA). For the TEM investigations, a JEM 2200 FS (JEOL, Japan) microscope operating at 200 kV was used. The conventional bright-field (BF) examination combined with the selected area diffraction (SAED) analysis was backed by the scanning transmission electron microscopy (STEM) imaging and high-resolution (HR) TEM observations powered by the Fast Fourier transformation (FFT) analysis.

2.2. AE analysis

Following the strategy proposed in [45], the continuously streamed AE data acquired during each loading cycle were sectioned into consecutive realizations of 8192 readings (of 4.1 ms duration) without overlapping. The AE Fourier power spectral density function (PSDF) $G_i(f)$ was calculated for each ith realization using a non-parametric Welch's method and normalized to the total (per realization) power $P_{AE} = \int_0^\infty G(f)df$ as given by Eq. (1) [45]:

$$\tilde{G}(f) = G(f)/P_{AE} \tag{1}$$

As a result of this procedure, a set of PSDFs was obtained and used for the classification of different types of soures of acoustic emission. A reasonable assumption, which serves as a prerequisite for the successful AE data partitioning and classification, is that different local stress relaxation mechanisms produce AE signals with different waveforms and, consequently, with different shapes of PSDFs [48]. Since multiple mechanisms of stress relaxation are anticipated during forward and reverse phase transformations upon loading cycles of the tested SMA single crystal, the recorded AE data were analyzed by a non-supervised adaptive sequential k-means (ASK) clustering algorithm [45] aiming at separating the contributions from different underlying processes (see also [39,46,47] for case studies). Mathematical details of the algorithm are presented in [45]. At variance with the conventional threshold-based signal detection, the ASK procedure identifies the signal as a fragment of the streaming data, which is statistically different from the pre-recorded background noise [45].

Two distinct and most important features, which highlight the key advantages of the ASK classifier if compared to many other methods such as the popular hierarchical k-means or c-means procedures, should be noted: (i) the number of clusters to be derived from a dataset is not specified a priori but is data-driven, and (ii) the process is non-iterative, i.e. the AE signals are sequentially associated with a particular cluster as they arrive one after another [45].

The primary goal of any clustering is to group similar and disjoint dissimilar objects. Therefore, a classifier requires a statistical measure of similarity/dissimilarity between objects. To this end, the normalized power spectra, Eq. (1), were used as input vectors for a pair-wise comparison and clusterization with a symmetrical version of the Kulback-Leibler (KL) divergence d_{KL} chosen as a statistical measure of similarity between two vectors $\tilde{G}_i$ and $\tilde{G}_j$, which is defined as [49]:

$$d_{KL} = \sum_{m=1}^{N} \left(\tilde{G}_{im} - \tilde{G}_{jm}\right) log\left(\frac{\tilde{G}_{im}}{\tilde{G}_{jm}}\right) \tag{2}$$

Using this metric, the algorithm calculates the mean distance $\bar{D}$ between all the class members $D(\tilde{G}_i, \tilde{G}_j)$, and its standard deviation σ_{GG}. A measure R of the intra-cluster distance is introduced as $R = \bar{D} + \alpha\sigma_{GG}$, where α is a constant having a value between 0 and 3. Finally, the AE signal is either assigned to an existing nearest cluster or becomes a seed for a new one.

3. Results

3.1. Stress-strain response

Fig. 1 represents the stress-strain response for different compressive loading cycles applied to the tested SMA single crystal. Fig. 1a reveals that the stress-strain behavior changes significantly from cycle to cycle. During the first cycle, pronounced irregularities are observed on the loading curve above the elastic limit, where the forward martensitic transformation occurs. These jerky features

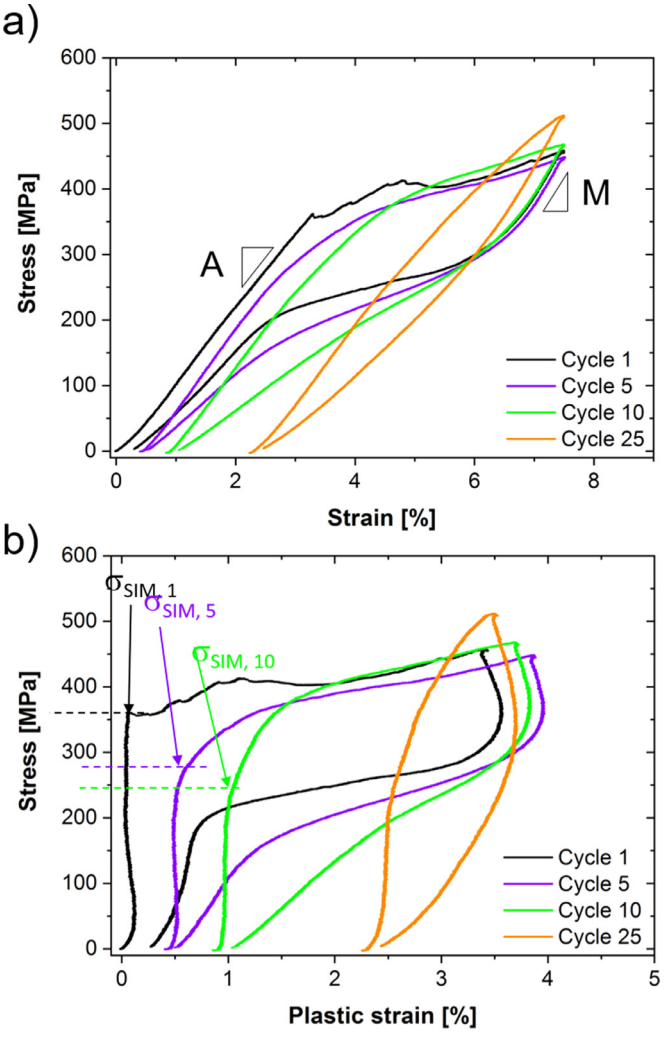

Fig. 1. (a) Compressive stress-strain response of the [00$\bar{1}$]-orientated Fe–Mn–Al–Ni SMA single crystal deformed in zero-compression mode up to 25 cycles. (b) Hysteresis loops in stress vs. plastic strain coordinates calculated by using linear slopes A for austenite and M for martensite. Critical stresses for SIM for the 1st, 5th and 10th cycle are indicated in (b).

tend to reduce with cycling and, finally, vanish after the fifth cycle. A plateau-like region due to the superelastic effect is observed with a certain slope in the loading curves until the fifth cycle. At a larger number of cycles, the plateau-like region shortens and finally disappears, indicating the progress in the cyclically-induced degradation of the superelastic effect.

For cycles 10 to 25, a non-symmetrical response with the evolution of a pronounced residual strain is seen in the stress-strain hysteresis. Concurrently, an increased significance of strain hardening can be recognized with the increase in the number of cycles. Furthermore, it becomes obvious that the slopes of the elastic regimes of the loading path and of the unloading path (i.e., at the load reversal point corresponding to the maximum strain value) are significantly different. This can be deduced from the stress vs. plastic strain plot (Fig. 1b). This plot was obtained after subtraction of the elastic component from the total strain; the slope within the linear regime of the austenite during loading corresponds to pure austenite during the 1st cycle, and autensite plus retained marteniste for all other cycles. However, the evaluated slope A (11.2 GPa for 1st cycle) clearly deviates from what is known from the literature reported for the austenite in a similar SMA alloy [50] (104 GPa and 61 GPa for the ⟨013⟩ and ⟨001⟩ orientations, respectively). This dis-

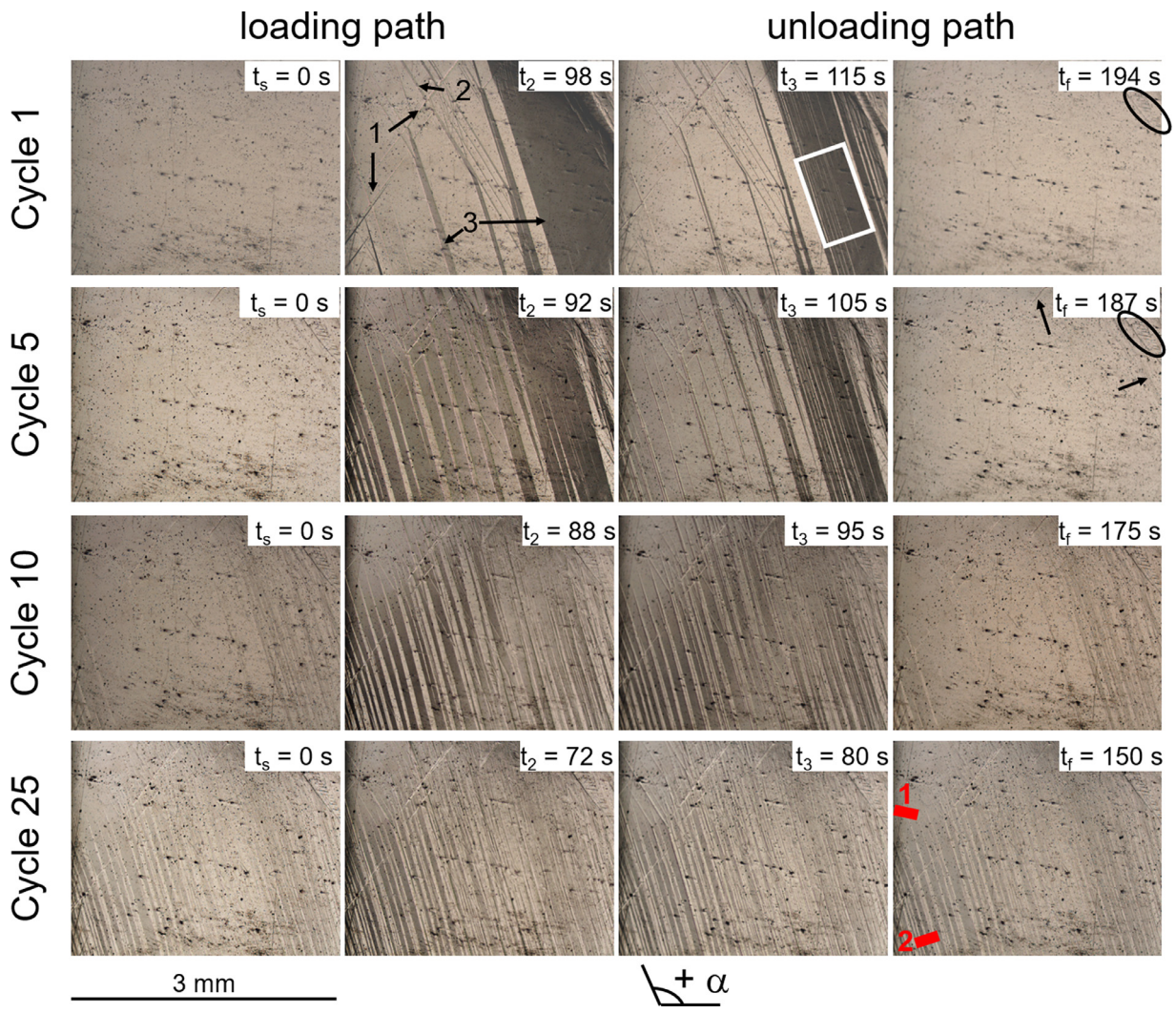

Fig. 2. Optical micrographs revealing typical surface features observed by microscopic video imaging during loading cycles 1, 5, 10 and 25, respectively. The loading direction is horizontal. The surface normal is aligned with the [1$\bar{1}$0] direction. Red regions labelled as 1 and 2 are areas where FIB lamellae were taken from for TEM investiagtions.

crepancy is caused by the way how the strain was measured via the crosshead displacement of the loading stage. Nevertheless, it is noticeable that the slope of the unloading part (M in Fig. 1a) is significantly different from A. For the first cycle, the linear slope M is about 15.2 GPa. As cycling proceeds, the slope of the linear loading part (A) increases to 13.5 GPa eventually pointing at the mixture of austenite and retained martensite being present already in the early stages of cycling. On the contrary, the slope of the unloading part (M) remains unchanged from cycle to cycle.

From the stress vs. plastic strain plot (Fig. 1b), it is possible to determine the critical stress (σ_{SIM}) for the stress-induced martensitic phase transformation (SIM). Evidently, the critical stress decreases with the increase of the number of cycles (Fig. 1b). Whereas the critical stress σ_{SIM} is about 360 MPa in the 1st cycle, this value reduces to 250 MPa and then to 200 MPa in the 5th and 10th cycle, respectively. In cycle 25, it is no longer possible to estimate the critical stress from the mechanical data.

A series of images shown in Fig. 2 illustrates the evolution of the transformation microstructure on the specimen's [1$\bar{1}$0] surface on the macroscale for both loading and unloading paths during cycles 1, 5, 10, and 25. In all cases, the crystal surface is shown at the start (t_s) and the end (t_f) of the loading cycle. The images at t_2 correspond to the end of the loading path (maximum strain), and images at t_3 were recorded shortly after the beginning of elastic unloading. Corresponding video records are provided in Supplementary Material Video 1 (1st cycle), Video 2 (5th cycle), Video 3 (10th cycle) and Video 4 (25th cycle).

Upon the initial loading, the first needle-like features related to the martensitic lath appeared on the crystal surface (pointed by arrows labelled with 1) with the inclination angle of $\alpha = 57$ ° (with positive values counterclockwise) to the loading axis at approximately $t = 35$ s. With good accuracy, this observation corresponds to the onset of the forward transformation regime on the stress-strain curve after elastic loading. Upon the increase in the compressive strain, more and more martensitic laths emerge on the crystal surface, as indicated by arrows 2 and 3 pointing to the traces of martensite variants having different orientations with respect to the loading axis (inclination angles of $\alpha = 121$ ° and $\alpha = 108$ °, respectively). As it is commonly observed in austenite–martensite phase transformations, the martensitic crystals nucleate heterogeneously and tend to appear in groups, i.e., the probability of nucleation is greater in the vicinity of a previously formed martensitic plate, cf. [35]. Before reaching the maximum compression load (at $t = 98$ s), a major martensitic lamella (indicated by arrow 3) forms and starts to grow smoothly in the lateral direction, spreading over a fairly large area. During unloading, numerous tiny areas within this sizeable transformed region start to transform back (cf. $t_3 = 115$ s, marked by the white rectangle). At the end

of cycle 1, only one small area with prominent remaining features, which can be most likely associated with retained martensite, was observed (cf. the elliptical mark, cycle 1, t_f).

At cycle 5, the first martensitic lath appeared on the crystal surface at $t = 52$ s. At the maximum load, which is reached at $t = 92$ s, the volume fraction of martensitic laths is significantly increased compared to the first cycle. Moreover, the martensitic phase transformation occurs being characterized by good reversibility during the first five cycles since only few macroscopically detectable small martensitic areas (indicated by arrows in Fig. 2, $t_f = 187$ s) remain visible on the crystal surface after unloading. The irreversibly transformed martensitic region retained after the first cycle again is indicated by the ellipse in Fig. 2 ($t_f = 187$ s). However, with the increasing number of cycles, the amount of martensite retaining after unloading increases progressively, cf. t_f in cycle 10. At cycle 25, virtually no changes, besides the small lateral movements of austenite/martensite interfaces, were observed on the surface during either loading or unloading. Thus, the *in situ* optical observations demonstrate evidently that martensitic transformation occurs in a non-reversible way towards a steady-state microstructure achieved after several loading cycles. This is fully corroborated by the evolution of the mechanical hysteresis showing a gradual transition from the strongly asymmetrical shape of the hysteresis loop characteristic of the superelastic behavior towards the almost symmetrical, but at zero load still fully closed hysteresis loop with a width of at least 1%. Thus, despite the preserved hysteretic behavior, the studied SMA single crystal exhibits a distinct functional degradation of superelasticity, continuously and rapidly evolving during compressive cyclic loading. The steady-state microstructure achieved after 25 loading cycles is discussed in the following section.

3.2. Microstructure after cyclic loading up to 25th cycle

The TEM and HR-TEM investigations carried out on FIB lamellae milled from regions with massive martensite transformation after the 25th loading cycle revealed a quite complex deformation microstructure. The regions where the two FIB lamellae were taken from were located at the left side of the region of interest shown in Fig. 2 (see red areas marked as 1 and 2). Both lamellae were cut perpendicular to the austenite/martensite interfaces macroscopically visible in Fig. 2 (cycle 25 at maximum load). At this stage, the macroscopic optical observations reveal a high amount of retained martensite in the test specimen. Since more than two different martensite variants were activated, intense interaction between different variants as well as between martensitic lamellae and dislocations occurred. Consequently, finding a correspondence between the macroscopic surface features and microscopic TEM images is hardly feasible. Thus, the TEM images shown below only represent an overview of the characteristic complex microstructure and details of individual features observed after 25 compressive cycles. Fig. 3 summarises the characteristic microstructural features observed on FIB lamella 1. Foremost, two major γ' martensite variants dominate the deformation microstructure of the bcc α−austenite matrix (cf. Fig. 3a marked by white arrows). These remaining martensite variants are quite thin (below 50 nm) and have a length of up to 1 µm. Some minor short martensitic segments are also visible in the TEM images (cf. light-grey arrows in Fig. 3a).

Austenite/martensite interfaces are pinned by parallel dislocations, as shown in Fig. 3b (white arrow), which is in good agreement with the results reported in [30]. The lower right corner in Fig. 3b represents a martensite lamella consisting of correspondent variant pairs (CVPs). The interaction between martensite variants is observed (Fig. 3a,c), which is supposed to be another factor (besides the parallel dislocations at the austenite/martensite interface)

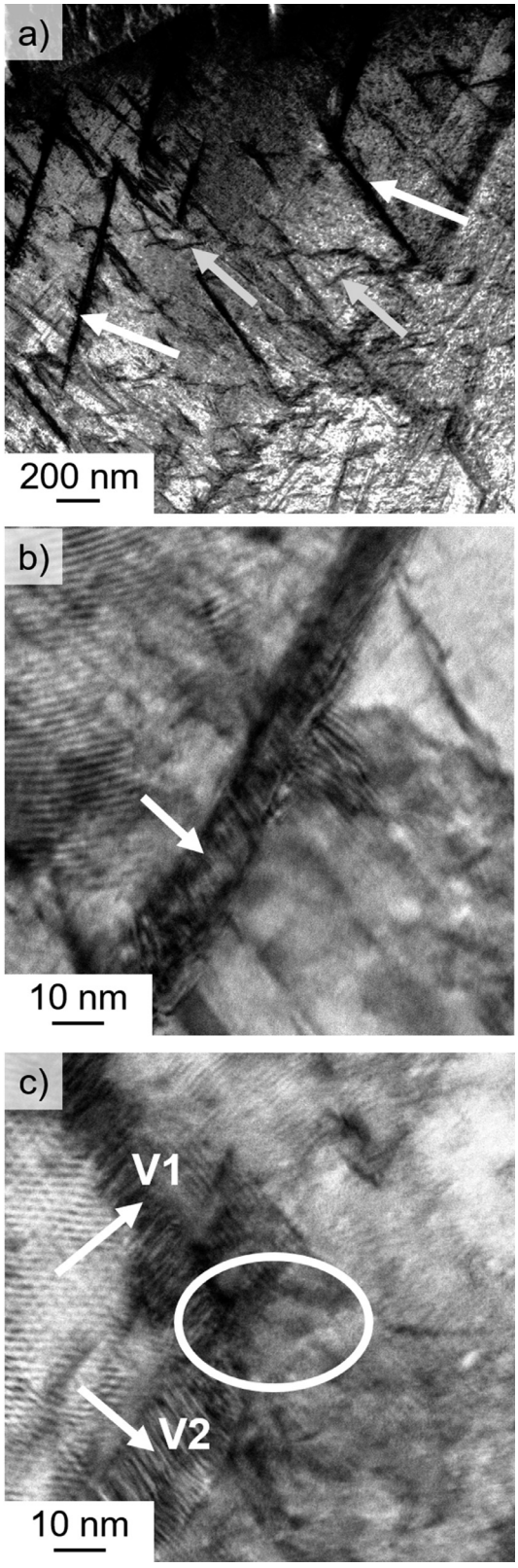

Fig. 3. TEM micrographs taken from FIB-milled lamella 1 after the 25th loading cycle in compression. (a) Different martensite variants (marked by arrows) interacting with each other. (b) Martensite variant with correspondent variant pairs (lower right corner) and dislocations pinned at the interface austenite/martensite (marked by the arrow). (c) Two intersecting martensite variants (V1, V2); the intersection area is marked by an ellipse.

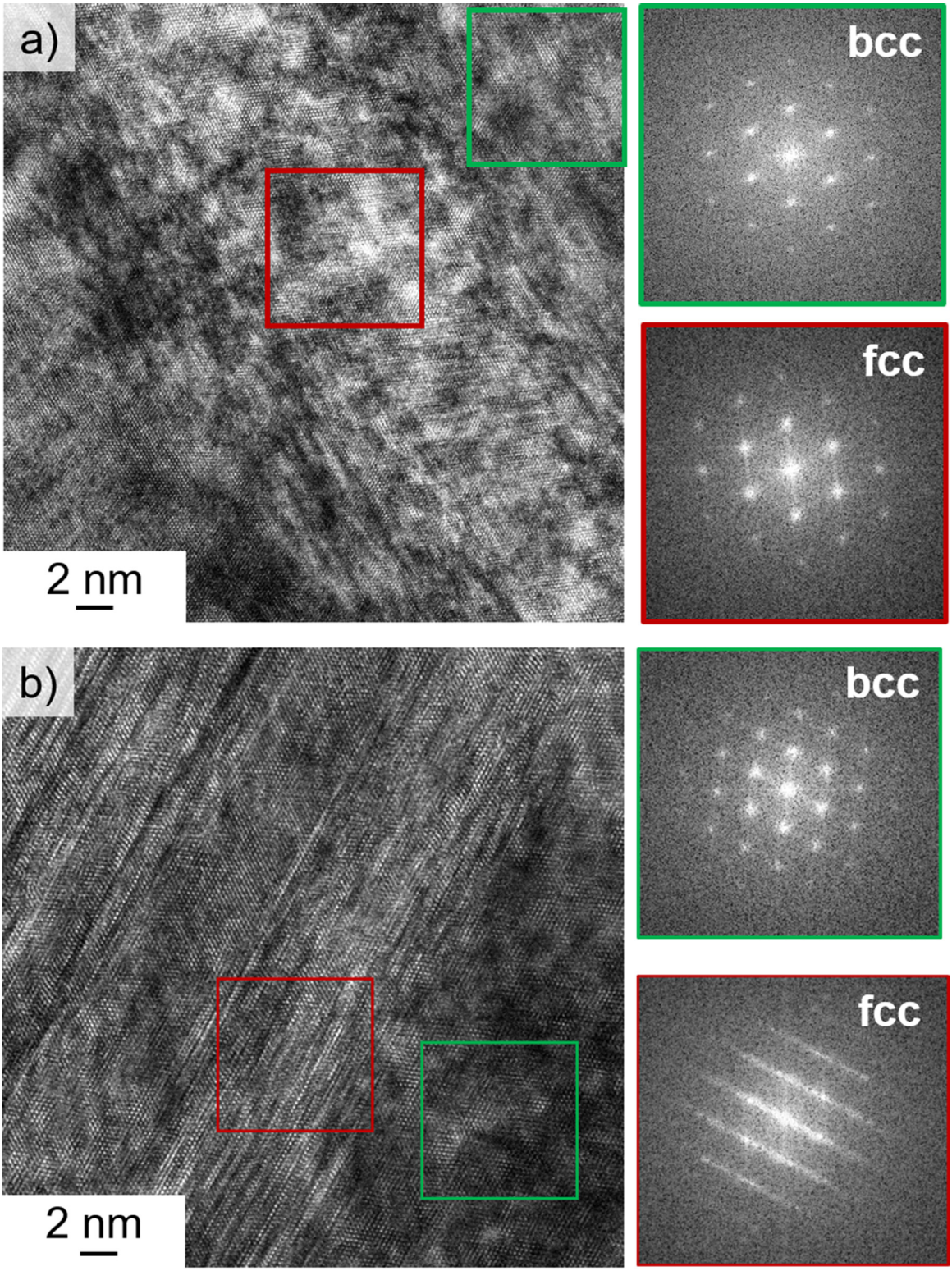

Fig. 4. HR-TEM images from the specimen after the 25th loading cycle. (a) FIB lamella 1: Martensite lamella (fcc) embedded in the bcc austenitic matrix, including FFTs of both areas. (b) FIB lamella 2: Martensite lamella (fcc) containing partial dislocations or nanotwins resulting in the streaks visible in the FFT image of the fcc martensite area.

affecting functional degradation of the superelastic effect in the investigated SMA single crystal.

Fig. 4 shows HR-TEM micrographs and corresponding FFT images of both the austenitic matrix (bcc) and a martensite (fcc) variant (Fig. 4a) as well as the internal structure of the martensite variant (Fig. 4b). Fig. 4b unveils the presence of partial dislocations or an indication of nanotwinned martensite [51]. These microstructural effects yield the streaking of the diffraction pattern shown by the FFT of the area marked by the red rectangle within the fcc martensite lamella. However, the individual dislocations and their interaction with precipitates can be hardly observed in the heavily distorted microstructure.

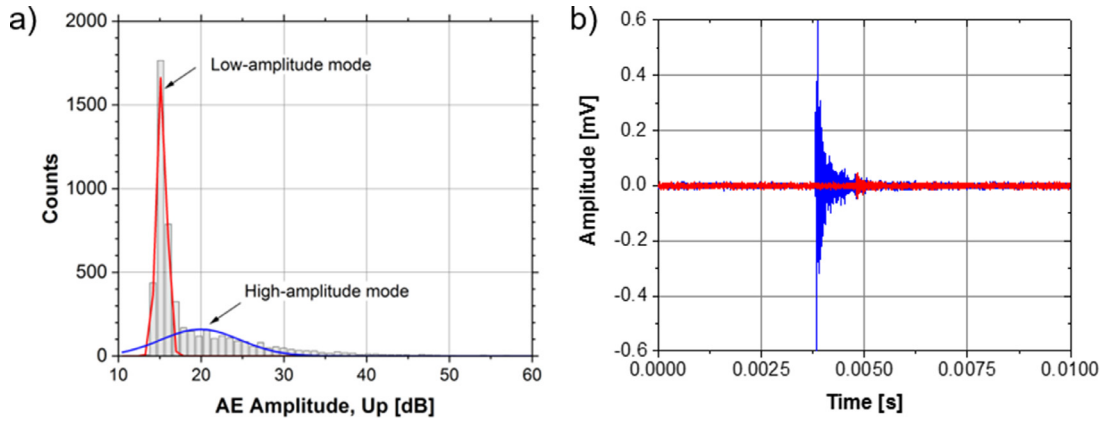

Fig. 5. Bi-modal histogram of AE amplitudes detected during cycle 1 (a) and two corresponding typical waveforms of AE signals on the background of laboratory noise: high amplitude transient signal (blue) and low amplitude signal (red) (b).

3.3. AE features in time and frequency domain

Remarkable changes in the deformation behavior and related mechanisms due to repeated loading are obvious not only from the mechanical data and microscopic observations, but also from the AE data. The distribution of the AE amplitudes detected throughout the first cycle appears to be bi-modal, see Fig. 5a. The experimental histogram can be reasonably approximated by a sum of two log-normal functions with different mean and variances characterizing two different populations of sources: (i) a high amplitude transient signal (blue) and (ii) a low amplitude signal (red) as shown in Fig. 5b.

AE records and their changes with cycling are represented in Fig. 6 separately for the loading and unloading paths. Fig. 6a shows two branches of the superelastic hysteresis loop, whereas Fig. 6b,c shows the corresponding raw AE data (Fig. 6b; note that only the positive parts of the streams are shown), and the AE activity (Fig. 6c), respectively, vs. time for cycles 1, 5, 10 and 25. One can notice that the AE streams consist of transient signals with broadly varying amplitudes. For all cycles, the amplitude scale remained the same (the incremental 2 V shift was applied for better visibility of individual plots). The AE activity λ was calculated as the number of AE events N detected by the ASK algorithm per unit time. For the 1st cycle, the stress-strain response and, independently, the AE analysis reveal three regions (A, B and C with subscript indexes L or U denoting loading or unloading parts of the hysteresis loop, respectively), which can be distinguished according to the features of the deformation curves or AE activity, and are indicated by vertical dashed lines.

On the loading part,

(i) Stage A_L is assigned to the elastic loading of the austenite. The AE is low and represented primarily by few weak signals similar to the noise level.
(ii) Stage B_L starts at the critical stress for martensitic phase transformation $\sigma_{SIM,1} = 360$ MPa and is assigned to stress-induced martensite transformation accompanied by pronounced serrations on the loading diagram and the high amplitude transient AE signals. The AE activity λ is quite high in this region, and peaks are revealed between 3 and 6% strain.
(iii) Stage C_L is characterized by a progressive, nearly linear increase in the stress accompanied by the rapidly increasing activity of AE transients peaking again between 6.5 and 7.5% strain.

In a similar way, the unloading path can also be conventionally divided into three regions:

(i) Stage C_U is related to the unloading of the stress-induced martensite. This part is surprisingly characterized by a large number of AE transients. However, their amplitudes are notably smaller than those during loading. The AE activity is maximal at the onset of the unloading stage, and then it decreases with the decreasing stress/strain.
(ii) Region B_U corresponds to the plateau region of the superelastic hysteresis loop, which is generally assigned to the reverse transformation of SIM [52]. This part is characterized by continuous AE signals of the scale comparable to the background noise resulting in the low detectable AE activity.
(iii) Finally, A_U is the elastic unloading of the austenite, which is accompanied again by low amplitude transient AE signals resulting in an increase of the AE activity in this region.

As cycling proceeds, significant changes occur in the deformation-induced processes as is witnessed by the AE data: the number and the amplitude of AE transient signals decrease drastically, and, concomitantly, the distribution of these transients along the loading and unloading paths changes too. High amplitude transient signals, which are abundantly present in region B_L in cycle 1, are much less significant during further cycling, and they disappear entirely at cycle 25. In region C_L, i.e., close to the maximum strain and stress, a large number of transient signals emerge during cycle 1, which then vanish with cycling. On the 25th cycle, only few low amplitude transient signals were recorded in the loading path. Similar behavior is reflected by the AE activity, which progressively decreased with cycling. It is important to notice that, in contrast to the loading path, a substantial contribution of AE transients was systematically recorded for all cycles upon unloading in region C_U while region B_U is characterized primarily by continuous signals resulting in very low overall activity. Finally, only during the first five cycles, the appreciable amount of low amplitude transients was also recorded in region A_U resulting in some measurable AE activity.

One should bear in mind that the integral AE activity incorporates contributions from all possible sources regardless of their origin. In order to get a deeper insight into the structure of the AE time series and to discriminate between different mechanisms governing the mechanical behavior, the signal clustering algorithm ASK [45] was applied to all data streams. This procedure revealed that the AE time series were not homogeneous for all investigated cycles. The AE signals fall naturally into three statistically representative groups characterized by their specific waveforms and corresponding PSDFs. Multiple descriptive features can be extracted from both time and frequency domains [53]. The example of data categorized in the AE energy E vs. median frequency f_m coordinates

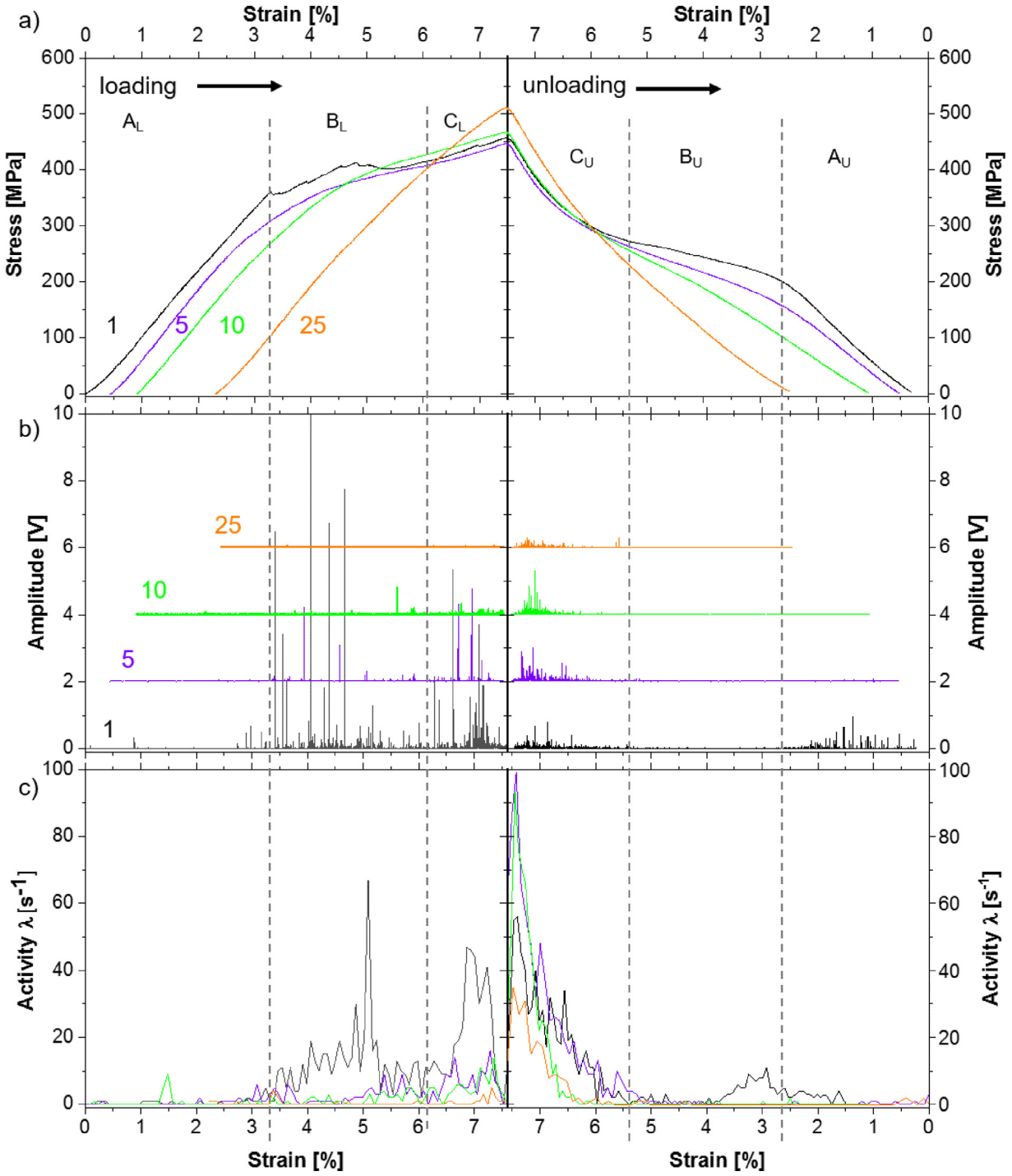

Fig. 6. Stress-strain responses (a) and AE data (b,c) for 1st (black), 5th (purple), 10th (green), and 25th (orange) cycles separated into loading (left) and unloading (right) parts. (b) Positive components of raw AE data streams showing AE amplitudes as a function of strain. (c) AE activity λ cacluated as a fucntion of strain. Stages of the deformation process are designated as follows: A_L-elastic deformation of austenite, B_L-stress-induced martensitic phase transformation, C_L-formation of SIM or (de)twinning, C_U-superelastic unloading of martensite, B_U-back transformation of martensite, A_U-elastic unloading of austenite (and retained martensite for the larger number of cycles); subscript *L* stands for loading and *U* for unloading.

is shown in Fig. 7 for cycles 1 and 25. The good separation between two classes of signals is apparent, i.e. the differences in the choosen features are significant enough to conclude that Clusters 1 and 2 are statistically different. Of course, other coordinates can be used for the 2D representation of the clustered data structure (see Supplementary Material S1 for respective examples). However, one should bear in mind that the ASK classifier is based on the entire PSDF shape and not on any combination of descriptive variables chosen for illustrative purposes.

The waveforms corresponding to laboratory noise were pre-recorded before the test, and their characteristic features remained unchanged until the test was terminated. They were, thus, automatically identified by the ASK algorithm and removed from the analysis. Two clusters differed from the noise and from each other according to their PSDFs were systematically discriminated by the

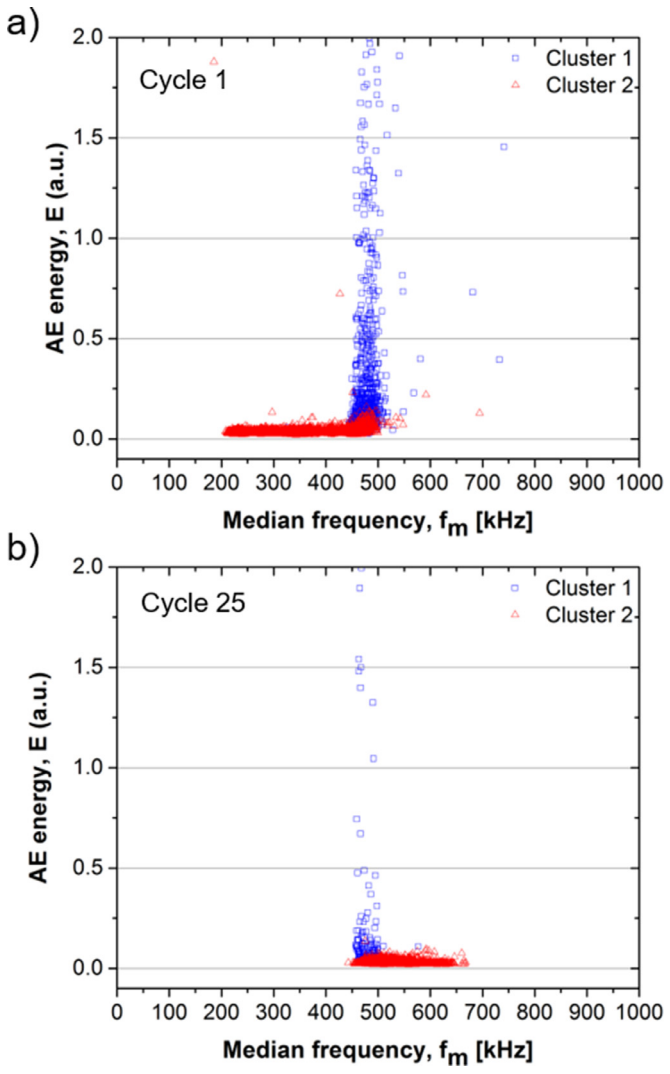

Fig. 7. Bi-variate E vs. median frequency f_m scatter-plots revealing the clustered data structure based on the PSD shape classifier for cycle 1 (a) and cycle 25 (b); data points are coloured with respect to their cluster numbers assigned during classification.

clustering algorithm during the entire testing campaign. Signals belonging to Cluster 1 (blue symbols, cf. Fig. 7) are high amplitude transients with the PSDF characterized by the high energy (power) and the median frequency around 470 kHz, whereas the signals from Cluster 2 (red symbols) appear primarily as low-amplitude bursts embedded into the continuous background noise (compare Fig. 5) yielding a wider PSDF with low energy (power) and widespread median frequencies as shown in Fig. 7. Since the ASK algorithm is based on the data-driven clustering procedure, the analysis of the behavior of different AE clusters was first performed in a non-supervised way without pre-justice and pre-interpretation of the labelled data. Once the features of each cluster have been established and their evolution with cycling is understood, the association and interpretation of underlying mechanisms are conducted.

Besides the two different AE sources being related to the two clearly distinct categories of AE signals, the cluster analysis revealed significant variations in the AE behavior during the loading and unloading stages. These differences can be easily traced by the evolution of E vs. f_m distributions as shown in Fig. 8 for Cluster 1 and Cluster 2 plotted separately for loading (filled symbols) and the unloading (open symbols) sections of different cycles (note the vastly different AE energy scales for the two clusters).

One can notice that not only the frequency ranges and the compactness of the clusters, which is determined by the variance of frequencies, are strikingly different for both major AE clusters–cf. compact Cluster 1 centred around f_m = 470 kHz and wide-spread Cluster 2 – but also the AE energy associated with the members of these clusters is remarkably different. The average energy of signals from Cluster 2 is significantly lower compared to those from Cluster 1 in each cycle. Besides, Cluster 1 exhibits significant differences in the AE energy for the loading and the unloading paths: the AE energy during unloading is significantly lower (by up to two orders of magnitude or more) than upon loading.

Both AE clusters evolve in response to the cyclically-induced microstructural changes, though apparently in different ways and to a different extent as represented in Fig. 9 through the average (per cycle) of the median frequency and the cumulative (per cycle) AE energy E_Σ plotted versus the number of cycles for both clusters. Although both clusters exhibit a gradual reduction of the energy of their members, the kinetics of these changes is notably different. The energy of Cluster 1 members reduces slowly during the first 7 cycles when the superelastic effect is most pronounced. However, in the subsequent cycles, the cumulative AE energy of Cluster 1 reduces steadily in parallel with the degradation in the superelasticity (although E_Σ does not diminish entirely). The cumulative energy of members of Cluster 2 drops significantly after the first cycle, and then it changes only slightly up to cycle 10 before it turns to decrease notably again. The frequency content of the Cluster 1 members remains practically unchanged (see the behavior of f_m in Fig. 9a). This behavior is in sharp contrast to that of Cluster 2, which shows the considerable shift of the AE PSDF to a higher frequency domain as reflected by the progressively increasing spectral median frequency f_m with the increasing number of cycles, cf. Figs. 8 and 9b.

3.4. AE data and deformation mechanisms

Fig. 10 summaries the behaviors of both AE clusters for the representative cycles 1, 5, 10 and 25 in terms of the cumulative AE energy E_Σ (bold lines) together with the loading and unloading parts of the hysteresis loops (thin lines). It should be noted that E_Σ is displayed with logarithmic scales identical for the loading and the unloading paths for better comparability. In cycle 1, signals from both clusters appear with the beginning of region B_L in perfect agreement with the initiation of the stress-induced martensitic phase transformation (Fig. 10a, b). The most rapid accumulation of members in Cluster 1 coincides with the serrations in the stress-strain diagram, which are accompanied by high amplitude bursts of high activity, cf. Fig. 6. A second much less pronounced increase in E_Σ is observed in region C_L up to the maximum strain value of 7.5%. For Cluster 2, E_Σ increases only moderately in region B_L; however, it exhibits a more pronounced increase in region C_L. During unloading, E_Σ increased as well, however, to a smaller extent as compared to the loading part. Clearly, the highest activity is observed in both clusters immediately after the load reversal (region C_U). Due to literature, this stage is associated with the elastic unloading of martensite [52]. However, the AE behavior represented in Fig. 6 does not leave any doubt that this stage is not entirely elastic. Thus, some microstructural processes reflected by high-energy transient signals occur in region C_U despite its "elastic" appearance. Interestingly is that in region B_U, related to the reverse phase transformation with a large amount of strain, the activity of both clusters reduces significantly. Finally, only minor AE is observed for both clusters in region A_U during the elastic unloading of austenite.

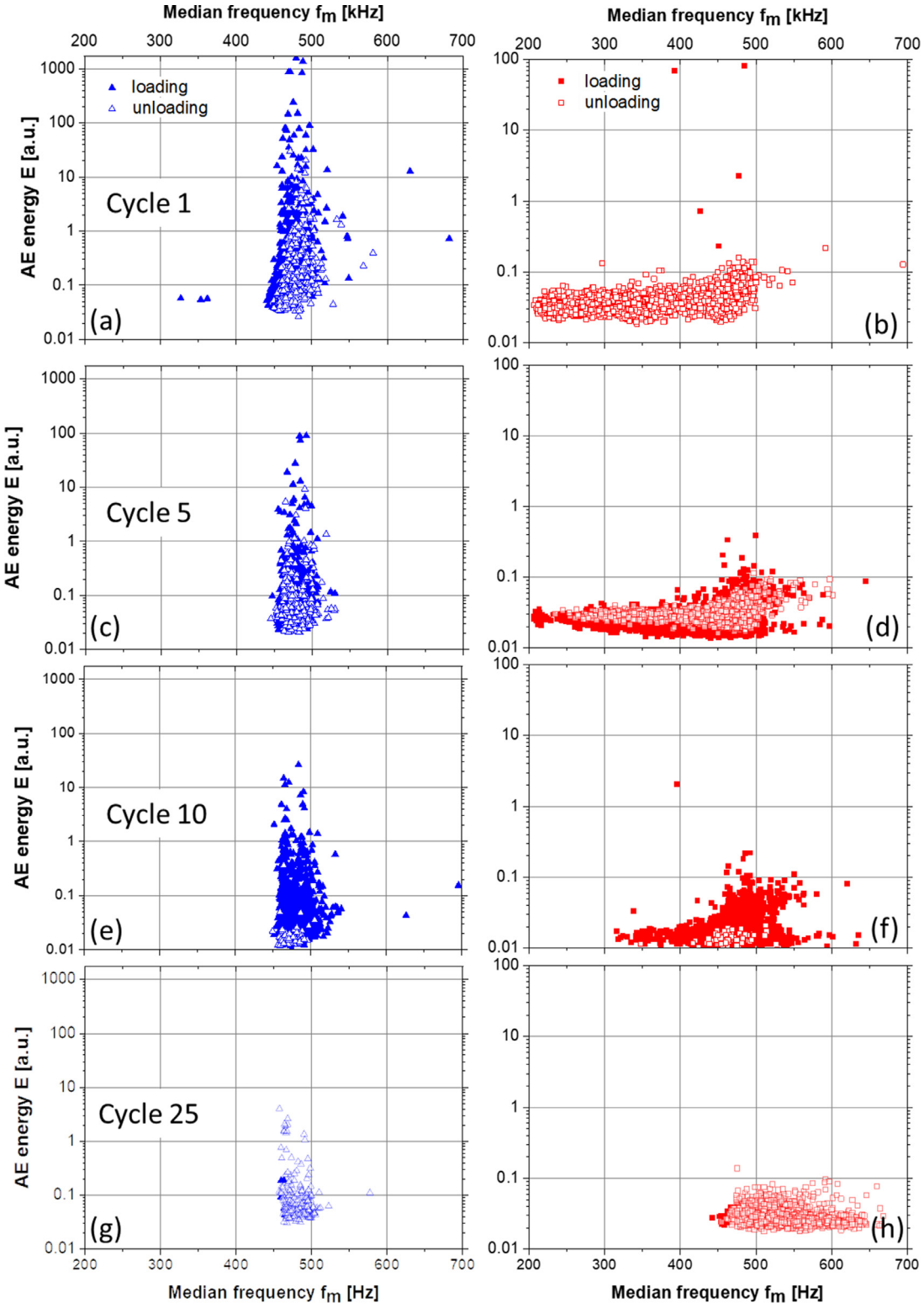

Fig. 8. Bi-variate scatter-plots of the AE energy E vs. median frequency f_m representing Cluster 1 (a,c,e,g) and Cluster 2 (b,d,f,h) separated for the loading (filled symbols) and the unloading (open symbols) paths for different cycles: (a,b) cycle 1, (c,d) cycle 5, (e,f) cycle 10, and (g,h) cycle 25.

As cycling proceeds (cf. cycle 5), the onset of both AE clusters is still observed in region B_L; however, it shifts to the lower stress values. The increase of E_Σ in region B_L is only moderate for both clusters. However, a more pronounced increase is observed for both clusters in region C_L. Concurrently, E_Σ was significantly smaller for both clusters compared to cycle 1. The cumulative energy E_Σ of Cluster 1 dropped in cycle 5 (Fig. 10a) by more than one order of magnitude compared to cycle 1. During unloading, in region C_U for both clusters again, an increase in cumulative energy E_Σ can be observed, which is zero in regions B_U and A_U.

The situation changes significantly in cycle 10. Here, in region B_L only small activity of Cluster 2 is detected. Cluster 1 starts to

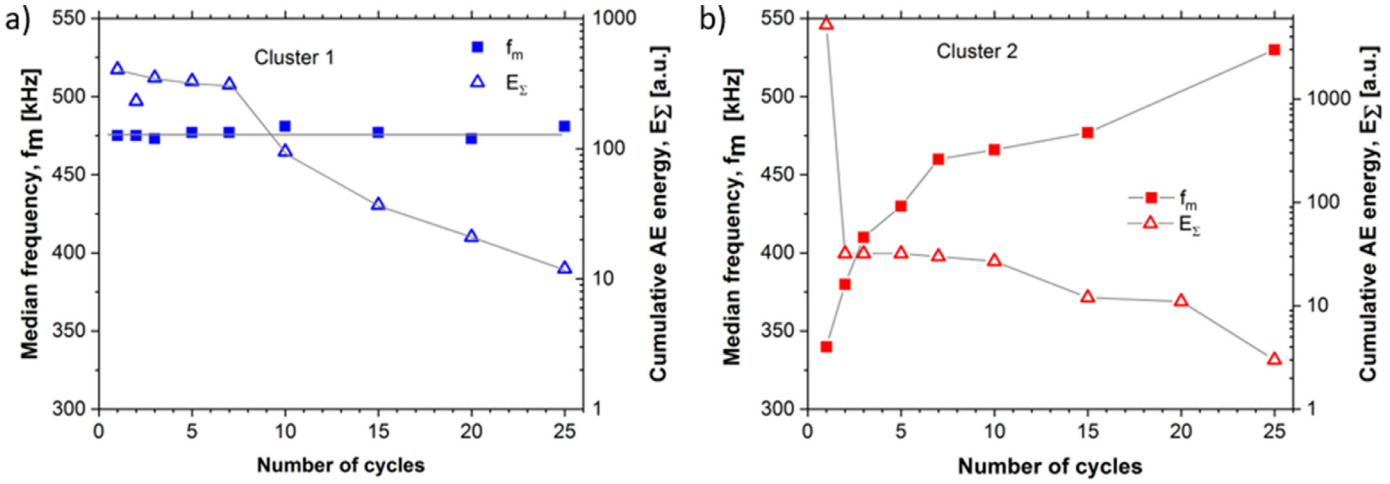

Fig. 9. Evolution of the median frequency f_m (filled symbols) of the centroids of two clusters and the cumulative AE energy E_Σ (open symbols): (a) Cluster 1; (b) Cluster 2.

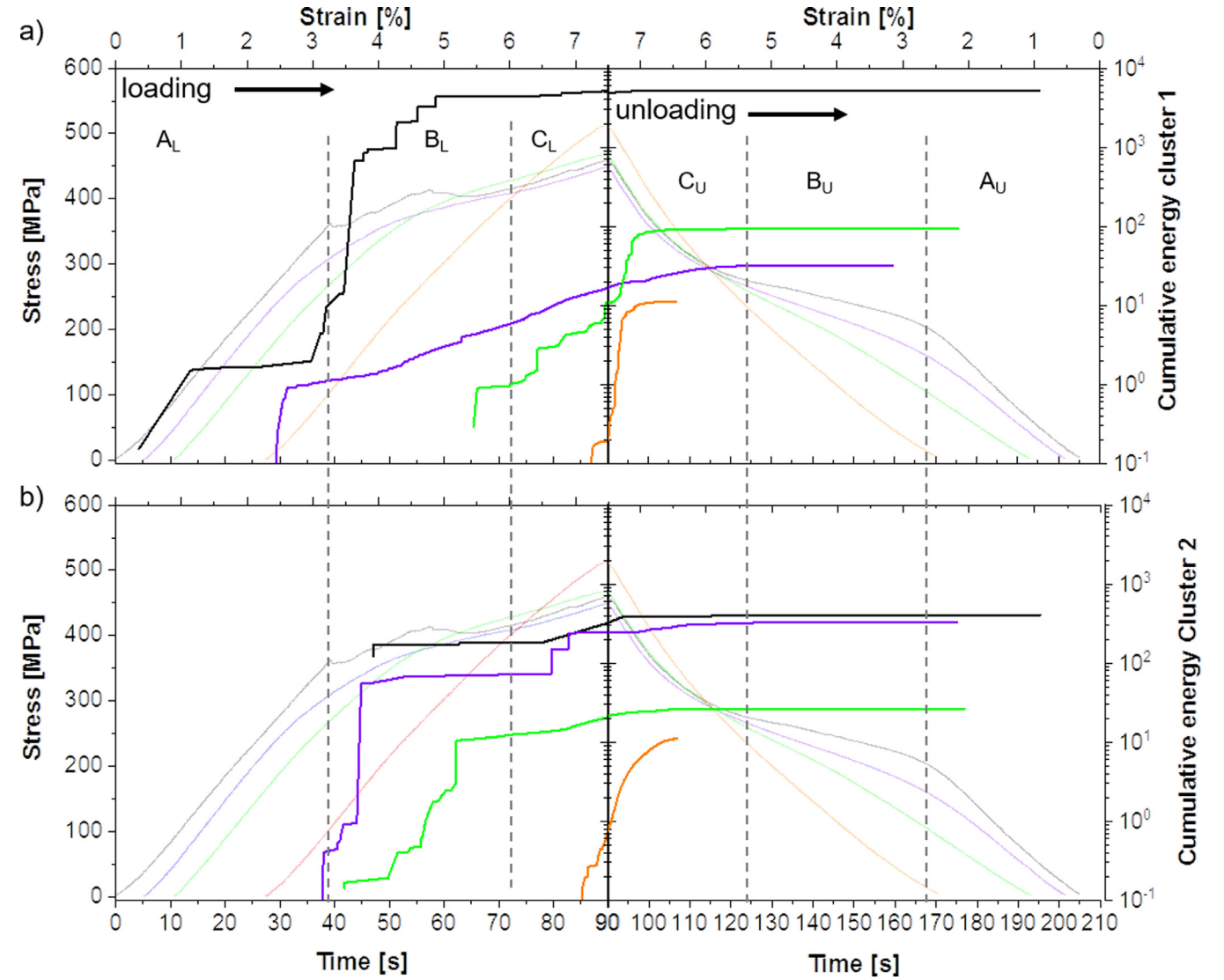

Fig. 10. Evolution of the cumulative AE energy E_Σ of Cluster 1 (a) and Cluster 2 (b) during cycles 1 (black), 5 (purple), 10 (green) and 25 (orange) over the entire loading cycles separated into the loading and the unloading path. The stress-strain hysteresis parts are indicated as well (thin coloured lines). In addition, stages of the deformation process are indicated, compare Fig. 6. Note the logarithmic scale for the cumulative AE energies of both clusters.

appear only at the end of region B_L and is more pronounced in region C_L. Compared to cycle 5, E_Σ was again by one order of magnitude smaller. However, during unloading, a remarkable increase in E_Σ of both clusters is observed in region C_U. As before, the E_Σ magnitude of Cluster 2 is significantly lower as compared to Cluster 1.

At cycle 25, the activity of both clusters is reduced to a very low level during the loading path, though it is not nullified. Both clusters are observed only in region C_L very close to the maximum strain of 7.5%. Surprisingly, both clusters exhibit some non-negligible amount of cumulative AE energy E_Σ generated immediately after the reversal point in the unloading path in region C_U.

4. Discussion

4.1. General remarks

Considering the distinct differences between the features in the AE signals belonging either to Cluster 1 or 2, their sources must be substantially different, too. The consensus seems to be reached in the community that acoustic emission signals with high-frequency content and high power (energy) are related to fast dynamic processes such as brittle crack initiation, twinning or diffusionless martensitic phase transformations [31]. In contrast, signals with lower frequencies and relatively low energies are related to the processes with slower dynamics such as dislocation motion or Lüders band propagation [54].

In the present case, the signals belonging to Cluster 1 are most likely related to martensitic phase transformation and, possibly, twinning. Cluster 1 starts during cycle 1 precisely at the critical stress of the SIM transformation and is observable only in region C_L close to the maximum strain value of 7.5% at the larger number of cycles. This hypothesis is further corroborated by the statistical analysis of the AE amplitude distributions compared to the distribution of surface features related to martensitic lamellae, as demonstrated in Fig. 11. Fig. 11a shows the martensite laths (dark contrast) formed during the 1st cycle up to the maximum compression load. The distinct martensite features were labeled one by one, and their width was measured in the direction perpendicular to the austenite/martensite interface (the open-source ImageJ image processing and analysis software package was used for this purpose). Fig. 11b reveals the probability density function distributions obtained independently for both the width of martensite lamellae (orange) and the amplitudes of AE signals (blue) ascribed to Cluster 1. The random variables (AE amplitude, U_p, and the width of the martensite plate, w_m) have been normalized to unity, i.e., related to the maximum value in the entire dataset. One can notice that the log-normal law can reasonably approximate both histograms. The fact that both empirical histograms are similar, yet not identical quantitatively, is neither surprising nor disappointing since AE is more sensitive to the rapid martensite phase initiation than to the relatively slow thickening stage. That is why the distribution peak for the AE amplitudes appears at slightly lower values when compared to the distribution of w_m. Even though this juxtaposition of two probability density functions cannot serve as proof of the assumption that both distributions have been generated by the same underlying process, Fig. 11b rather supports than contradicts this hypothesis. At the higher number of cycles, reliable determination of the width of individual martensite lamellae based on optical micrographs becomes impossible and, thus, has not been carried out.

Signals belonging to Cluster 2 show, however, a marked shift of the median frequencies from lower to higher values with cycling (cf. Figs. 8 and 9). This is what is typically observed and plausibly expected for dislocation-mediated plasticity and can be understood in terms of the reduction of the mean free path of dislocations

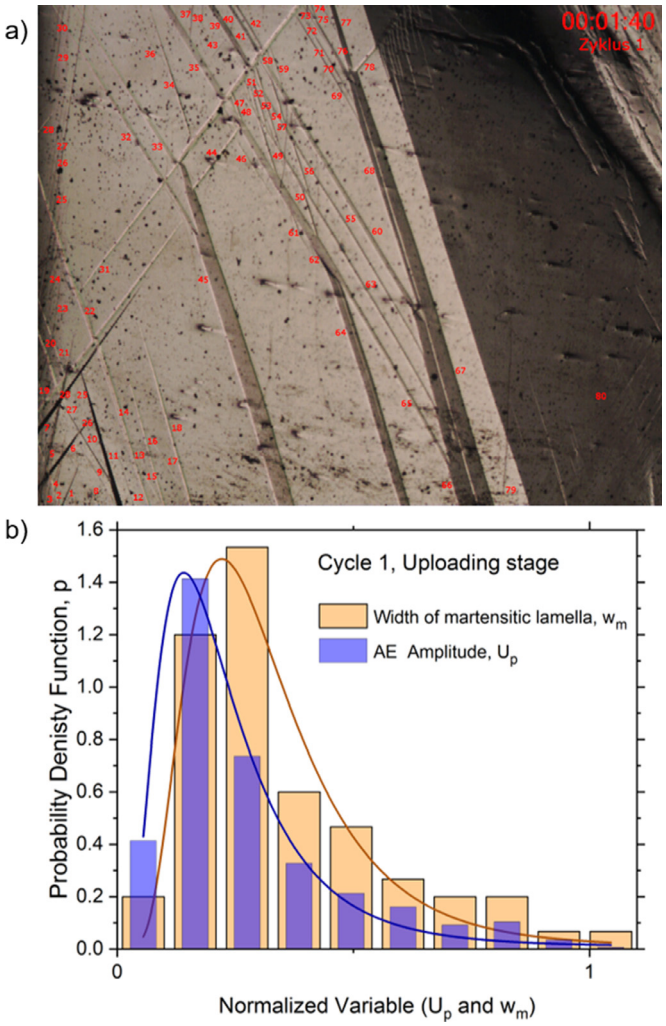

Fig. 11. Correlation of AE results and martensite formation. (a) Optical micrograph of the surface of the single crystal showing martensite lamellae formed during the 1st loading cycle up to maximum compressive load. Individual lamellae are numbered. (b) Probability density functions vs. normalized parameters of AE peak amplitude U_p and width of martensitic lamellae w_m.

[55]. In a similar way, the observed behavior of Cluster 2 can be interpreted in terms of the progressive fragmentation of the microstructure by the increasing fraction of martensite upon cycling. Thus, Cluster 2 can be attributed to the propagation of the austenite/martensite interfaces of martensite variants and coupled dislocation motion. In both cases, the mean free path is reduced due to the rapid fragmentation of the microstructure in the course of SIM.

Finally, it can be stated that at least two fundamentally different microstructural mechanisms have been identified by the AE analysis. The marked functional degradation of the superelastic effect within 25 compressive loading cycles is undeniably reflected by AE data. A conclusive discussion on AE findings in conjunction with the evolution of the cyclic stress-strain response and the surface topography will be given in Section 4.3.

4.2. Interpretation of microstructural observations in relation with the stress-strain responses

The microstructure of the investigated Fe-Mn-Al-Ni single crystal consists of the bcc austenitic phase with fine β-precipitates (enriched in Ni and Al) exhibiting a B2 structure [30]. Ojha and Sehitoglu have suggested that the martensitic phase transformation in this microstructure is an inverse fcc-bcc transformation, which

occurs by a two-step shear mechanism [56,57]. Since the phase transformation proceeds from bcc α-austenite to fcc γ'-martensite, the two-step shear processes involve partial dislocations moving on different slip planes. Thus, a perfect dislocation of the bcc lattice has to split into three partial dislocations according to the following reaction: $\frac{a}{2}[1\bar{1}1] = \frac{a}{8}[0\bar{1}1] + \frac{a}{4}[2\bar{1}1] + \frac{a}{8}[0\bar{1}1]$. The first shear operation is carried out by the movement of partial dislocations of type $b = \frac{a}{8}[0\bar{1}1]$ on each {110} lattice plane, and the $\{110\}_{bcc}$ plane transforms into $\{111\}_{fcc}$, accordingly. This is followed by a second shear operation of partial dislocations with $b = \frac{a}{6}[1\bar{2}1]$ on each third $\{111\}_{fcc}$ lattice plane [55]. However, the lattice structure created after this martensitic phase transformation does not represent the perfect fcc lattice [58]. Recently, Fischer et al. [59] showed by extensive EBSD analyses that the martensite in Fe-Al-Mn-Ni SMA can be described as a nanotwinned fcc lattice structure, which is tetragonally distorted (presumably face centred tetragonal-fct). Tseng et al. [51,60] reported a strong dependence of the reversibility of the martensitic transformation on the formation of twinned or detwinned martensite. Orientations showing single (detwinned) martensite variants exhibit poor reversibility, whereas orientations where twinned martensite is observable show good reversibility. According to Tseng et al. [61], the theoretical values of the formation strain of CVPs and the detwinning strain under compression are identical (10.5% for the ⟨001⟩ orientation). Thus, the crystal with the $[00\bar{1}]$ orientation investigated in this study is able to accommodate the compression strain by at least two equivalent variants resulting in good reversibility [61].

Considering the fact that the microstructure contains nanosized precipitates, the role of these precipitates during martensitic phase transformation has to be taken into account as well. To this end, two scenarios are discussed in the literature depending on the size of precipitates, which were proposed by Maki and Wayman [62], who considered the martensitic phase transformation of γ'-precipitates in the Fe-Ni-Ti-C alloys. The first scenario assumes that the precipitates also undergo a martensitic phase transformation [62]. According to the second scenario, the precipitates remain in their initial (austenitic) lattice structure [62]. The critical factor triggering the martensitic phase transformation of precipitates is their size [62]. As long as the precipitates are small enough, they tend to transform into martensite. Maki and Wayman [62] suggested a critical size of about 5 nm for γ'-precipitates in Fe-Ni-Ti systems. Precipitates with dimensions above 5 nm should remain austenitic. In line with these discussions, Omori et al. [63] showed for the alloy Fe-Mn-Al-Ni that ß-precipitates (B2) with a size of 10 nm do not transform into martensite during thermal cycling. Although these precipitates do not transform, they exhibit coherency to the fcc martensite. They are, however, slightly distorted, and the distortion angle remains the same in the fcc martensite. Therefore, no misfit dislocations are observed at the interfaces of precipitates during thermal cycling between austenite and martensite. The internal stresses caused by β-precipitates are elastically accommodated by nano-twinning of the martensite [63]. However, the recent investigations by Walnsch et al. [64] on thermally induced martensite on Fe-Mn-Al-Ni SMAs with different chemical compositions gave new insights into this topic by showing that the coherent B2 precipitates transform together with the austenitic matrix. The resulting martensitic microstructure consists accordingly of fct matrix and precipitates with the $L1_0$ crystal lattice structure [64].

The results of the present study concerning the stress-strain response at a constant temperature above the austenite finish temperature A_f during the first cycle are in good agreement with abundant literature data. For the investigated alloy, it is plausibly to expect that misfit dislocations, as well as partial dislocations, appear during the formation of stress-induced martensite. Partial dislocations are readily seen on the TEM images shown in Fig. 4b. The misfit dislocations generated during mechanical loading in the austenitic phase in the vicinity of martensite variants emerged as a consequence of the partial irreversibility and are manifested by parallel dislocation arrangements seen in TEM micrographs shown in Fig. 3b. However, due to the highly distorted microstructure after 25 loading cycles, their individual features can hardly be resolved. Thus, more detailed cycle-by-cycle TEM examinations are required for the in-depth understanding of the microstructural evolution, which are beyond the scope of the present study.

The cycle-dependent stress-strain response of the single crystal tested in the present work can be divided into three consecutive stages, cf. Fig. 1: Stage 1-cycles 1 to 5, Stage 2-cycles 6 to 15, and Stage 3-cycles 16 to 25 based on the visual difference between the shapes of the cyclic hysteresis curves indicating the progress of functional degradation. In Stage 1, the classical SE hysteresis loop is observed. In the 1st cycle, the critical stress for martensitic transformation is reached at about 360 MPa. Beyond this point, a distinct superelastic strain region (see B_L in Fig. 6a) is formed, which is featured by distinct serrations accompanied by an audible sound. These serrations are caused by the formation of large martensitic plates extending throughout the entire cross-section of the specimen, leading eventually to significant stress fluctuations as reported in [65]. At around 5% strain corresponding to a stress value of 400 MPa, no further serrations are seen. However, a pronounced increase in the stress is observed, accompanied by the smooth lateral growth of the martensitic plates being present. After deformation to the maximum pre-set strain of 7.5%, the unloading starts, and the reverse transformation stress is reached at about 300 MPa. The superelastic plateau during the reverse transformation is smooth, and austenite appears in response to the reverse transformation in numerous small areas within the large martensitic plates. From cycle 1 to cycle 5, the forward transformation stress decreases progressively from 360 to 250 MPa. The irreversible strain accumulated during the first five cycles is relatively small (i.e., about 0.5%). The characteristic serrations during the forward transformation decrease in number and magnitude with cycling and, finally, disappear entirely within 5th cycle. These experimental findings are in good agreement with the results reported in the literature [55,60,65,66]. According to Tseng et al. [26], 400 MPa corresponds to the critical stress for martensitic transformation in ⟨001⟩-orientated FeMnAlNi SMA single crystals under compression loading. Combining the present findings with the literature data, it can be assumed that the SIM (of twinned martensite) is the main active process responsible for the superelasticity during the first five cycles. However, the decrease in the critical stress for martensitic transformations and remaining martensite undeniably indicate the beginning of functional degradation, for which several reasons are known: (i) pinning of the martensite/austenite interfaces by precipitates, (ii) pinning of martensite/austenite interfaces by dislocations formed at the interface for strain compensation, and (iii) interaction between differently orientated martensite variants [30].

Stage 2 is characterized by the significant reduction of the superelastic plateau strain, which is accompanied by the further decrease in the critical SIM stress down to 200 MPa (at 10th cycle), significant strain hardening up to the final stress of 500 MPa and a pronounced increase in the irreversible strain. The reverse transformation stress remains stable at 300 MPa.

In stage 3, the superelastic strain plateau vanishes. No transformation stress can be determined anymore, and the irreversible strain increases to the maximum of 2.5% for a given number of loading cycles. The peak stress increases by 60 MPa (up to 510 MPa), which is likely linked to the martensitic phase transformation of new areas as it has been reported in [28,30]. In cycle 25, the superelastic effect is practically exhausted. Nevertheless, some superelasticity beyond the Hooke's law region can still be recognized, yielding a markedly opened stress-strain hysteresis and eventually reversible strain of about 1%. A similar effect was ob-

served in NiTi SMA and termed "twinning elasticity" or "twinning-induced elasticity" (TIE) [67]. In the past, it was also reported as 'linear superelasticity' [68,69] or 'twinning pseudoelasticity' [70]. Hornbogen [70] argued that TIE in NiTi relies on the growth and shrinkage of stabilized martensite variants. The hypothesis made by Hornbogen is that this effect is not related to the phase transformation anymore. Instead, it is supposed to be caused by the stabilization of martensite twins and the mobility of twin boundaries. In consequence, the martensite twin variants with favourable orientations grow at the expense of others during loading. This reorientation process occurs when the external stress becomes larger than the internal stress fields caused by the stabilizing dislocation substructure. With a decrease in stress during unloading, the dislocations stress fields again dominate and eventually restore the original twinned martensite. Birk et al. [67] reported on 3% of reversible strain caused by TIE in pre-deformed NiTi wires. Zheng et al. [68] confirmed by *in situ* TEM investigations on NiTi wires that twinning and detwinning (microtwins) occurring in stabilized martensite variants during loading and unloading, respectively, is the microscopic mechanism for the TIE effect. However, the mechanism of TIE has not been well understood yet. In the present work, the studied Fe-Mn-Al-Ni alloy seems to show an effect similar to the TIE at the larger number of compression cycles ($N > 15$). Here, it can be assumed that internal stress fields affect the formation of variants [28]. This implies an increasing dislocation activity leading to the stabilization of twinned martensite, eventually leading to TIE. However, further investigations are crucially needed to reveal the prevailing mechanisms since it is not clear at this point why the alloy should show TIE in this particular orientation since no additional elongation can be accommodated due to detwinning.

Undoubtedly, the stress-strain response of the [00$\bar{1}$] orientated Fe–Mn–Al–Ni single crystals undergoes a cycle-dependent change from a fully reversible superelasticity ($N = 1$) to partially-reversible superelasticity ($2 < N < 5$) followed by a high degree of irreversibility ($6 < N < 15$) and, finally (and presumably) TIE ($N > 15$).

The above-described characteristics of the stress-strain response of Fe-Mn-Al-Ni single crystals strained under compressive load for 25 cycles are supported by the video observations of the surface of the specimen and the independent acoustic emission measurements. In this regard, the video surface observations reveal significant changes in the transformation behavior after the first loading cycle already. Fig. 12 shows characteristic surface images of the same field of view from the video streams at $t = 65$ s (loading path) for the first cycle (Fig. 12a) in comparison to cycles 2 (Fig. 12b) and 10 (Fig. 12c). The crystallographic orientation of the single crystal during the surface observations is shown on the inset in Fig. 12c. During the first cycle, two habit plane variants on nearly symmetrically arranged planes (10$\bar{1}$) and (011) with trace angles of $\alpha = 121\,^\circ$ (dashed white line) and $\alpha = 57\,^\circ$ (bold white line) with respect to the loading axis were observed macroscopically on the specimen surface (positive trace angles α, counterclockwise). Both systems (10$\bar{1}$)[111] and (011) [11$\bar{1}$] show the highest calculated Schmid factors of $\mu = 0.45$. The thickness of these two habit plane variants is relatively tiny. In addition to the two symmetrical habit plane variants, one more system is observed, which becomes dominant upon further loading.

The trace angle for this variant at the specimen surface is $\alpha = 108\,^\circ$ with respect to the loading axis, and thus can be correlated with the ($\bar{1}$10) plane. However, the Schmid factor is very low for the system ($\bar{1}$10)[111] ($\mu = 0.13$). In contrast to the two symmetrical variants, the laths seen are much thicker. They dominate the later deformation process by growth and shrinkage (see Fig. 12b and c, and video1 in the Supplementary Material). In addition, Fig. 12d–f show three sequential images of the surface taken during the first cycle at 66 s, 67 s, and 68 s, respectively, at the position marked in Fig. 12a. It is obvious that the very tiny lamellae parallel to the (011) plane appear prior to those on the plane ($\bar{1}$10). In the region of interaction, the appearance of the SIM arranged parallel to ($\bar{1}$10) is fan-shaped. With the increase of strain during the first loading cycle, this SIM variant dominates and exhibits a pronounced lateral growth (cf. Fig. 2). With the increasing number of cycles, the occurrence of the two symmetrical variants (10$\bar{1}$) and (011) becomes rare on the macroscopic scale. Finally, they are no longer activated after the fifth cycle. Instead, the variant with the inclination angle of $\alpha = 108\,^\circ$ becomes dominant on the macro-scale. In cycle 10 shown in Fig. 12c, mainly this variant is visible in optical microscopy. The activation of the martensitic variant with the lower Schmid factor can only be understood in terms of the complex local internal stress state most probably caused by the nanosized β-precipitates and by the previously transformed martensite [28,30].

However, another interpretation could arise from the fact that the trace angle of this variant is close to the trace angle of $\alpha = 94\,^\circ$ of a ($\bar{1}$11) plane (for the sake of clarity not indicated in Fig. 12a). The {111} planes are involved in the motion of partial dislocations with $b = \frac{a}{4}\langle 112\rangle$ during the second shear operation step necessary for the bcc/fcc phase transformation [55]. The Schmid factor for the system ($\bar{1}$11)[$\bar{1}$1$\bar{2}$] is $\mu = 0.5$, and is, therefore, higher than that for SIM on the systems (10$\bar{1}$) [111] and (011) [11$\bar{1}$], respectively ($\mu = 0.45$). This could implicate that these very pronounced lamellae belong most probably to the slip system of Shockley partial dislocations in the formed martensite that is almost fcc in nature.

The video surface observations during the unloading part reveal another important fact: the reverse transformation sets in already at the very beginning of unloading. Fig. 13a shows the loading and unloading path of cycle 1 plotted in combination with the calculated AE activity λ (compare Fig. 6a, c). The high AE activity during unloading in region C_U can be at least in part directly correlated with the onset of reverse transformation right at the beginning of the unloading. The surface images shown in Fig. 13b were taken at the points indicated on the load-time curve. Whereas points 1 and 2 are related to the end of the loading and the onset of the unloading stages, respectively, points 3 to 6 are located in the unloading part C_U, which is expected to be the elastic unloading of the SIM. However, the images in points 3 to 6 clearly reveal numerous tiny areas where the reverse transformation already occurred.

4.3. Interpretation of AE sources

Many differences in the acoustic emission signals generated during forward and reverse transformations have been noticed in numerous prior publications. Planes and Vives [71] discussed the apparent asymmetry of the AE activity during forward and backward transformations in CuZnAl and FePd single crystals occurring concurrently with differential scanning calorimetry (DSC) measurements in terms of the difference between the nucleation in the forward austenite → martensitic transformation and the fast shrinkage of martensitic domains in the reverse martensite → austenite transformation. In other words, these authors argued that the asymmetry originated from the differences in the nucleation processes. On the other hand, Beke et al. [72] suggested an alternative energy-based interpretation of the observed asymmetry in the forward/reverse transformations during DSC experiments. The vast majority of results confirm that AE during the forward austenite → martensite transformation was less pronounced in terms of the number of counts/events and their amplitudes than those measured during the reverse martensite→austenite transformation for various SMA systems [33,40,73–80].

A clear asymmetry in the forward and reverse transformations was also observed in the AE data of present study (cf. Figs. 6, 8, 10). However, new insights can be uncovered in AE data by using

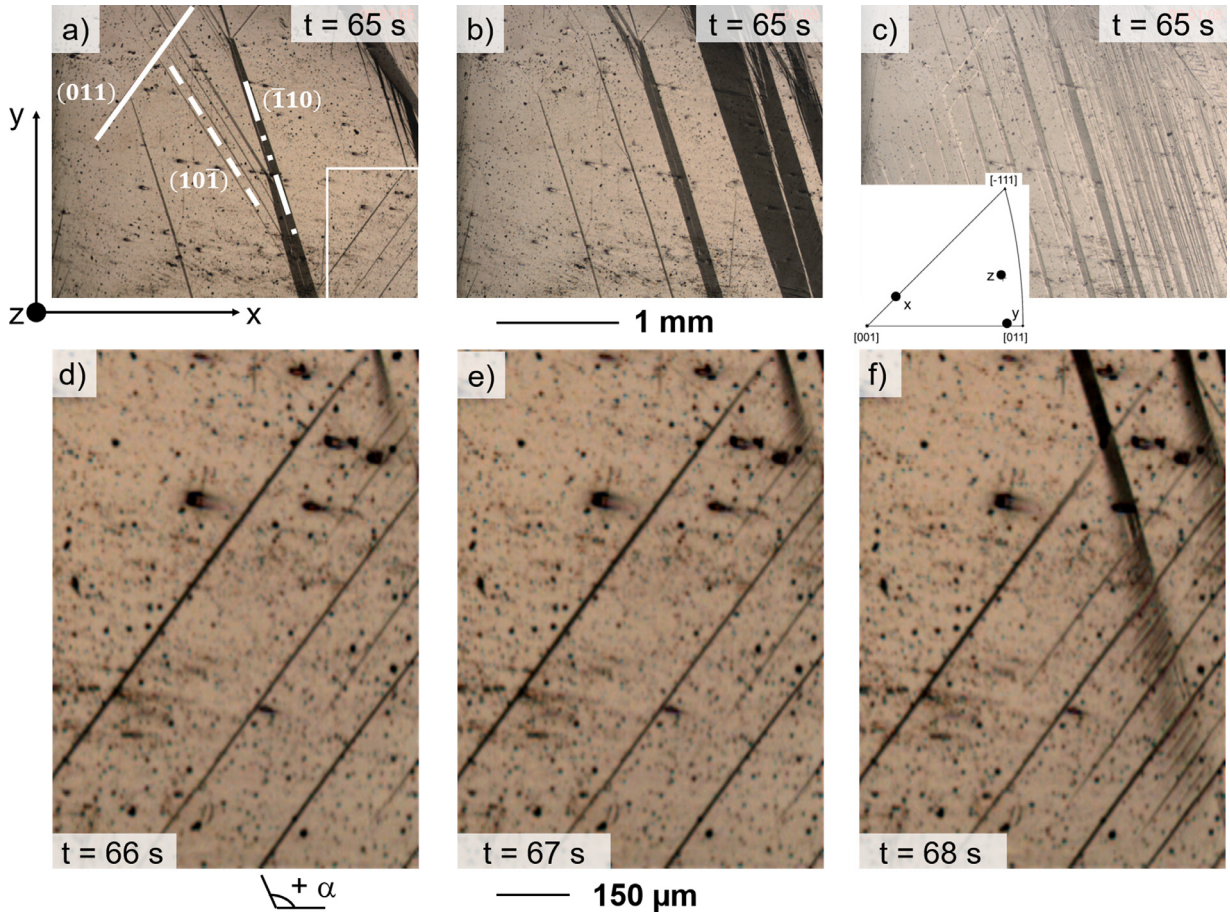

Fig. 12. Surface images illustrating the changes in activation of martensite variants in a [00$\bar{1}$] single crystal of Fe-Mn-Al-Ni SMA under compressive cyclic loading. (a) Cycle 1. (b) Cycle 2. (c) Cylce 10. (d–f) Higher magnification of the area marked in (a) at t = 66 s (d), t = 67 s (e), and t = 68 s (f) in cycle 1.

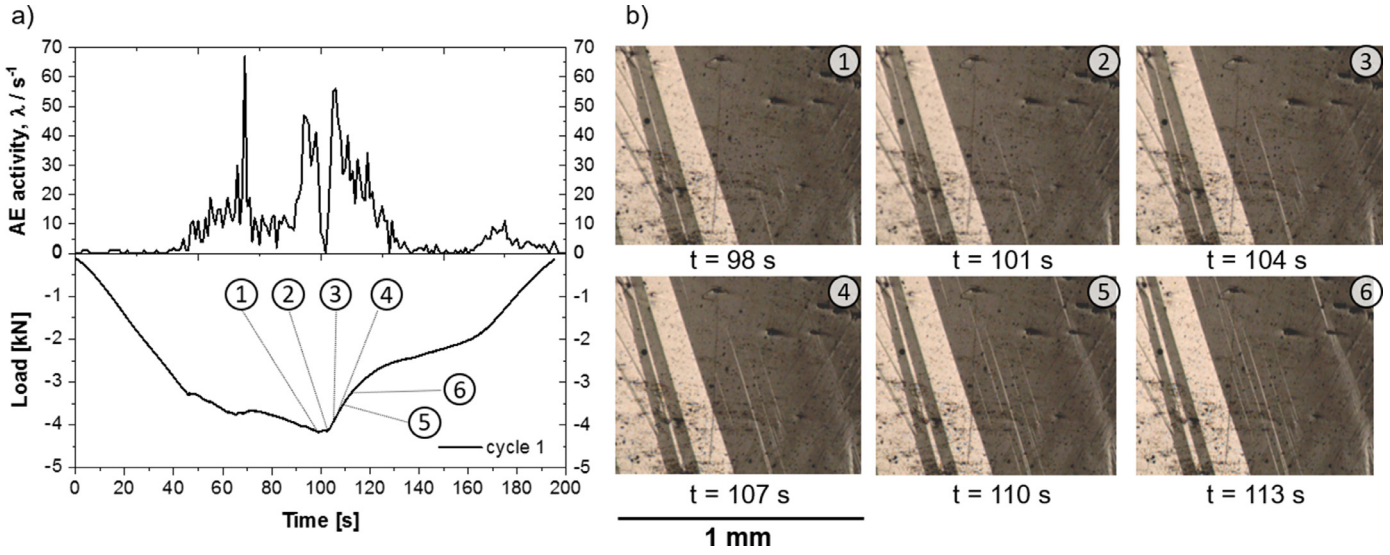

Fig. 13. Surface images (b) illustrating the onset of the reverse transformation at the selected points during the load history of cycle 1 (a) combined with the calculated AE activity λ.

the statistical clustering procedure, which will be discussed in the context of the mechanical and microstructural behavior in the remainder of this work.

Fig. 14 provides a schematic description of changes in the superelastic response of the studied Fe-Mn-Al-Ni single crystal and the related interpretation of AE data in the context of functional degradation for the first cycle with superelasticity and a later cycle after high functional degradation.

Starting with the first cycle (Fig. 14a) and the initial austenitic microstructure (point 1) containing nanosized coherent precipitates, the elastic deformation of austenite occurs in region 2. Two symmetric SIM variants (μ = 0.45) appear on the crystal surface

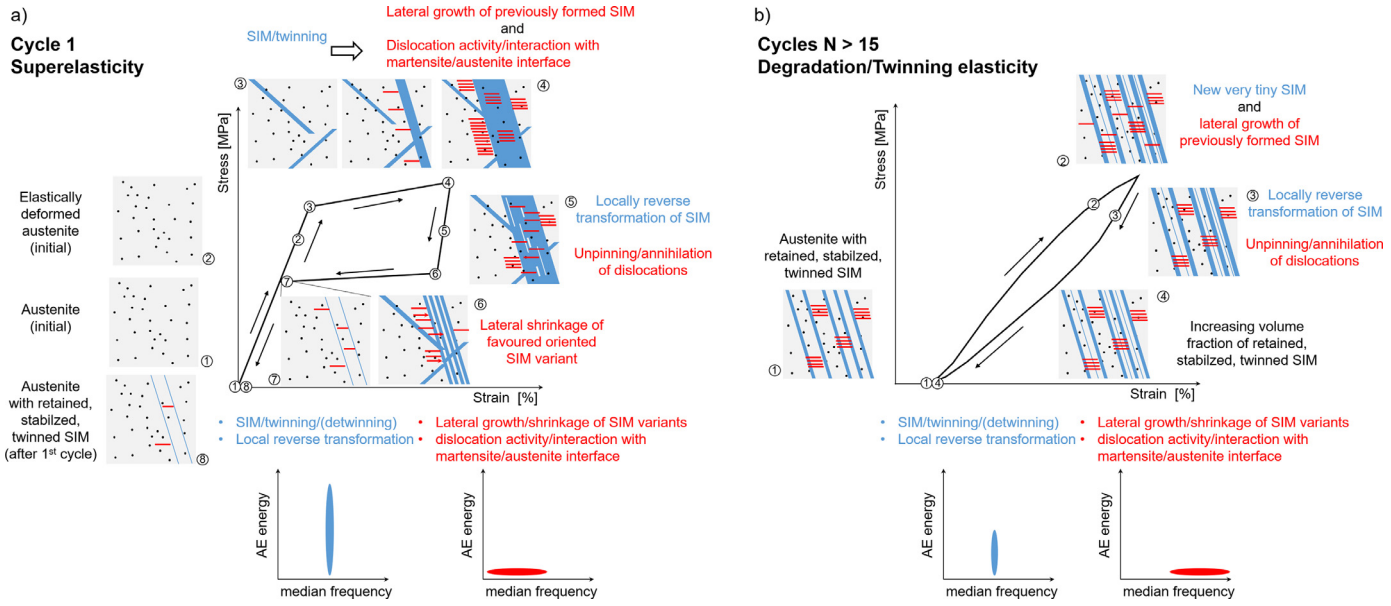

Fig. 14. Schematic description of changes in the superelastic behavior of Fe-Mn-Al-Ni SMA under compressive loading combining stress-strain response, surface observations and acoustic emission measurements. (a) Cycle 1. (b) Cycle $N > 15$.

immediately when the transformation stress σ_{SIM} is reached (point 3). This process is accompanied by audible sound, which is also detected by the high-frequency AE sensor. Soon after the formation of the two symmetric variants, a third variant starts to develop under a trace angle of $\alpha = 108\ ^\circ$ (being different from the former ones), which interacts with the previously formed symmetric SIM variants.

With high confidence, the AE Cluster 1 can be related to the formation of SIM. This cluster comprises members with the high energy E in a very narrow band of median frequencies f_m around 470 kHz (cf. Fig. 8). The frequency distribution of this cluster practically does not change with cycling, while the energy and the number of events decrease significantly. However, only one of the SIM variants seems to be favourably orientated for lateral movement of the austenite/martensite phase boundary: only for the SIM variant with the angle of $\alpha = 108\ ^\circ$ the lateral movement of austenite/martensite interfaces is observed (point 4).

The movement of the interface resembling the Lüders-like behavior results in the appearance of AE Cluster 2 featured by its low energies. These low energy signals spread widely in the frequency domain (cf. Cluster 2, Fig. 8) and shift to higher frequencies as cyclic deformation proceeds. Low energies of AE signals are related to the relatively low velocity of the lateral interface motion. The observed shift within Cluster 2 to higher median frequencies is caused by the reduction in the mean free path for moving interfaces since the amount of martensite retained after each cycle steadily increases. Cluster 2, therefore, is deemed to be caused by the movement of transformation partial dislocations. The video records taken during the loading and unloading deformation stages unveil that the forward and reverse transformations occur strongly asymmetrically. As opposes to the above-described scenario for the loading path, the movement of the whole interface of the favourably orientated large SIM variant is not observed upon unloading. Instead, the backward transformation occurs at different sites within the large martensitic plates; it is, therefore, restricted to small volumes. This process leads to the splitting of the large favourably orientated SIM variants into smaller fragments. The comparison of video sequences with the stress-time plots shows that the SIM fragmentation process commenced immediately after the onset of unloading (cf. point 5 in Fig. 14a). This process is again associated with the high-amplitude AE Cluster 1 exhibiting the temporal evolution in excellent agreement with the video data. In addition, the shrinkage of fragmented regions is observed (indicated by red arrows at point 5). After reaching the stress level for the backward transformation in the superelastic hysteresis loop (point 6 in Fig. 14a), the shrinkage of the remaining martensitic areas prevails in the deformation region and governs the stress-strain response. In parallel, the activity of dislocations stabilizes the martensite. Both these mechanisms can be collectively ascribed to low-energy Cluster 2. Finally, the stabilized martensite remains in the austenite and the fraction of retained martensite increases cycle-by-cycle.

With the increase in the number of cycles (Fig. 14b; $N > 15$), the favourably orientated SIM variant ($\alpha = 108\ ^\circ$) tends to prevail over the others, whereas the thickness of the individual martensite lamella reduces progressively, indicating the degradation of the superelasticity caused by the stabilization of this favourably orientated SIM. This is obvious from (i) the decrease in the AE energy of Cluster 1 and (ii) the shift of members of Cluster 2 to higher frequencies.

The stable and compact Cluster 1 reflects the martensitic phase transformation causing the superelastic effect that determines region B_L of the hysteresis loop. Some members of the same cluster can also be associated with the twinning processes accompanying SIM formation. Since more and more martensite retains in the matrix after unloading due to martensite stabilization, the activity of Cluster 1 in region B_L reduces and, eventually, disappears with the increasing number of cycles (cf. cycle 25). Nonetheless, Cluster 1 is persistent in region C_L in harmony with the formation of martensite in new areas, as it has already been reported in [28,30]. It seems reasonable due to the increased peak stress at 7.5% strain, which could provide the additional driving force for nucleation of martensite in previously untransformed areas. However, it could also herald the aforementioned TIE effect, which is still questionable and has to be investigated in more detail in the future.

Although the amplitude (or energy) of the Cluster 1 members reduces steadily with cycling, the distribution of the AE energy over the entire frequency band in the PSD remains unaffected. The stability of the frequency distribution in the PSD implies that al-

though the intensities of transformation-related processes reduce with cycling (most probably due to functional degradation and stabilization of martensite), the dynamics of the underlying processes do not change substantially. Thus, these processes, i.e., martensitic phase transformation and/or twinning/detwinning processes, occur at essentially the same spatial and temporal scales, which makes it challenging to distinguish between them (at least, with the current experimental setup).

The behavior of Cluster 2 resembles the characteristics of dislocation slip during strain hardening of ordinary pure metals and alloys [54,55]. The AE caused by the stochastic dislocation motion is featured by a low-amplitude waveform and a wideband noise-like spectrum, which evolves to a high-frequency domain [54,55] when the dislocation mean free path decreases with strain hardening. Similar behavior is seen for Cluster 2 in Fig. 9b: (i) the shift of the signal to high frequencies, and (ii) the sharp initial drop of the average AE activity (per cycle) and the cumulative energy after the first loading cycle followed by the progressive decrease of these variables with cycling. However, the superposition of optical microscopic observations with the AE time series suggests that the fluctuating lateral movement of the austenite/martensite interface can account for the observed low amplitude wideband signals forming Cluster 2, cf. the movement of austenitic/martensitic interfaces of the major martensitic lamella labelled as 3 in Fig. 2. The video imaging was performed at a slow frame rate (100 fps) that did not allow resolving the details of the propagation of interface boundaries. However, this motion of the austenite/martensite interface is often described in analogy with the Lüders band collective phenomenon, e.g. in the NiTi shape memory alloys [81,82]. Thus, similarly to Cluster 1, there are two mechanisms related to Cluster 2 - dislocation slip and lateral movement of austenite/martensite interfaces - and it is hard to distinguish between them in the AE process since both mechanisms are similar in their dynamics, resulting in essentially the same class of signals.

Finally, it is conceivable that AE clusters are related to the following primary mechanisms operating at different times within the superelasticity hysteresis loop:

(1) Cluster 1 is related to SIM operating in regions B_L and C_L.
(2) Cluster 1 also receives members from the reverse transformation of small volume elements of SIM in region C_U.
(3) Cluster 2 originates primarily from the intermittent lateral propagation of martensite/austenite interfaces operating in regions B_L/C_L and B_U.
(4) Cluster 2 is also related to dislocation activities (movement, annihilation, unpinning from precipitates) in regions C_U and A_U (the distinction between these possible dislocation reactions is not possible with the present setup).

5. Summary

Superelasticity of the [00$\bar{1}$] orientated Fe-Mn-Al-Ni single crystal was investigated by *in situ* measurements of acoustic emission under compressive loading up to a nominal strain of 7.5% and 25 cycles. The pronounced functional degradation during cyclic loading was interpreted based on optical and transmission electron microscopy observations in combination with detailed AE data analysis in the frequency domain. The main findings can be summarized as follows:

(1) The investigated single crystal exhibits excellent superelasticity up to 7.5% of strain, which is, however, accompanied by a pronounced degradation; the degradation process is appreciable already during the first five loading cycles, which becomes more pronounced with further cycling until the last cycle, where the reversible strain is only of 1%.
(2) Both the stress-induced martensitic phase transformation, as well as functional degradation, were detected by acoustic emission.
(3) Two different types of AE signals with respect to their frequency and energy properties were unravelled: (i) high-energy signals within a narrow frequency band of about 470 kHz remaining constant over 25 cycles, and (ii) low-energy broadband signals tending to shift to higher frequencies with the increase in the number of cycles.
(4) Whereas signals belonging to the group (i) are related to SIM/twinning/detwinning, the signals of the group (ii) are related to the lateral movement of martensite/austenite interfaces and dislocation activities such as unpinning from precipitates or annihilation.
(5) A distinct asymmetry of the forward and reverse transformations was detected by acoustic emission measurements. Although the signals related to SIM/twinning/detwinning decrease significantly with the increasing number of cycles due to the increase in the irreversibility of SIM, the AE activity during the unloading path remains at a surprisingly high level, which is attributed to both dislocation activities and reverse transformation.
(6) Operating mechanisms responsible for functional degradation are known from the literature [28,30]. They include (i) the interaction of different martensite variants, (ii) generation of dislocations and their interaction with martensite/austenite interfaces, and (iii) the interaction of austenite/martensite interfaces with B2 precipitates. Even though these reactions can be reflected in the AE signal, the acoustic emission is an indirect method, and the direct TEM observations were performed only after the 25th cycle. Therefore, it is not possible yet to state conclusively where individual irreversible processes initiated and interacted. Thus, the individual contribution of each elementary mechanism to functional degradation has to be assessed in follow-up work.

Finally, the present investigations backed by the acoustic emission measurements and analysis provide the first insights into elementary processes including their temporal activation underlying superelasticity in FeMnAlNi SMA. However, further detailed investigations are required to clarify the kinetics of the irreversible processes and the asymmetry in the transformation behavior. To this end, TEM studies will be conducted after each loading cycle, and different types of iron-based SMAs will be examined for the sake of generality.

Declaration of Competing Interest

The authors declare that they have no known competing financial interests or personal relationships that could have appeared to influence the work reported in this paper.

Acknowledgment

Financial support of Deutsche Forschungsgemeinschaft (DFG, German Research Foundation) for the Collaborative Research Centre 'TRIP-Matrix-Composite' (CRC 799, project B5) under Project-ID 54473466 and projects 314279646 and 405372848 is gratefully acknowledged.

Supplementary materials

Supplementary material associated with this article can be found, in the online version, at doi:10.1016/j.actamat.2021.117333.

References

[1] P.S. Lobo, J. Almeida, L. Guerreiro, Shape memory alloys behavior: a review, Procedia Eng. 114 (2015) 776–783.
[2] J. Mohd Jani, M. Leary, A. Subic, M.A. Gibson, A review of shape memory alloy research, applications and opportunities, Mater. Des. 56 (1980–2015) (2014) 1078–1113.
[3] W.J. Buehler, J.V. Gilfrich, R.C. Wiley, Effect of low-temperature phase changes on the mechanical properties of alloys near composition TiNi, J. Appl. Phys. 34 (1963) 1475.
[4] L. Janke, C. Czaderski, M. Motavalli, J. Ruth, Applications of shape memory alloys in civil engineering structures-overview, limits and new ideas, Mat. Struct. 38 (2005) 578–592.
[5] R. Kainuma, Recent progress in shape memory alloys, Mater. Trans. 59 (2018) 327–331.
[6] A. Cladera, B. Weber, C. Leinenbach, C. Czaderski, M. Shahverdi, M. Motavalli, Iron-based shape memory alloys for civil engineering structures: an overview, Const. Build. Mater. 63 (2014) 281–293.
[7] T. Sawaguchi, I. Nikulin, K. Ogawa, K. Sekido, S. Takamori, T. Maruyama, Y. Chiba, A. Kushibe, Y. Inoue, K. Tsuzaki, Designing Fe–Mn–Si alloys with improved low-cycle fatigue lives, Scr. Mater. 99 (2015) 49–52.
[8] T. Sawaguchi, T. Maruyama, H. Otsuka, A. Kushibe, Y. Inoue, K. Tsuzaki, Design concept and applications of Fe–Mn–Si-based alloys-from shape-memory to seismic response control, Mater. Trans. 57 (2016) 283–293.
[9] H. Sehitoglu, I. Karaman, X.Y. Zhang, Y. Chumlyakov, H.J. Maier, Deformation of FeNiCoTi shape memory single crystals, Scr. Mater. 44 (2001) 779–784.
[10] Y. Tanaka, Y. Himuro, T. Omori, Y. Sutou, R. Kainuma, K. Ishida, Martensitic transformation and shape memory effect in ausaged Fe–Ni–Si–Co alloys, Mater. Sci. Eng. A 438-440 (2006) 1030–1035.
[11] S. Kajiwara, Characteristic features of shape memory effect and related transformation behavior in Fe-based alloys, Mater. Sci. Eng. A 273-275 (1999) 67–88.
[12] A. Sato, H. Kubo, T. Maruyama, Mechanical properties of Fe–Mn–Si based SMA and the application, Mater. Trans. 47 (2006) 571–579.
[13] A. Sato, E. Chishima, Y. Yamaji, T. Mori, Orientation and composition dependencies of shape memory effect in Fe-Mn-Si alloys, Acta Metall. 32 (1984) 539–547.
[14] A. Sato, E. Chishima, K. Soma, T. Mori, Shape memory effect in $\gamma \rightleftarrows \epsilon$ transformation in Fe-30Mn-1Si alloy single crystals, Acta Metall. 30 (1982) 1177–1183.
[15] K. Ōtsuka, C.M. Wayman, Shape Memory Materials, 1st ed., Cambridge University Press, Cambridge, New York, 1999.
[16] P.La Roca, A. Baruj, M. Sade, Shape-memory effect and pseudoelasticity in Fe–Mn-based alloys, Shape Mem. Superelasticity 3 (2017) 37–48.
[17] Y. Tanaka, Y. Himuro, R. Kainuma, Y. Sutou, T. Omori, K. Ishida, Ferrous polycrystalline shape-memory alloy showing huge superelasticity, Science 327 (2010) 1488–1490.
[18] T. Omori, K. Ando, M. Okano, X. Xu, Y. Tanaka, I. Ohnuma, R. Kainuma, K. Ishida, Superelastic effect in polycrystalline ferrous alloys, Science 333 (2011) 68–71.
[19] Y.U.N. Koval, V.V. Kokorin, L.G. Khandros, Shape memory effect in Fe-Ni-Co-Ti alloys, Fiz. Met. Metalloved. 48 (1979) 1309–1311.
[20] T. Maki, K. Kobayashi, M. Minato, I. Tamura, Thermoelastic martensite in an ausaged Fe-Ni-Ti-Co alloy, Scr. Metall. 18 (1984) 1105–1109.
[21] H. Sehitoglu, C. Efstathiou, H.J. Maier, Y. Chumlyakov, Hysteresis and deformation mechanisms of transforming FeNiCoTi, Mech. Mater. 38 (2006) 538–550.
[22] H. Sehitoglu, X.Y. Zhang, T. Kotil, D. Canadinc, Y. Chumlyakov, H.J. Maier, Shape memory behavior of FeNiCoTi single and polycrystals, Metall and Mat Trans A 33 (2002) 3661–3672.
[23] P.L. Roca, A. Baruj, C.E. Sobrero, J.A. Malarría, M. Sade, Nanoprecipitation effects on phase stability of Fe-Mn-Al-Ni alloys, J. Alloys Compd. 708 (2017) 422–427.
[24] J. Ma, B.C. Hornbuckle, I. Karaman, G.B. Thompson, Z.P. Luo, Y.I. Chumlyakov, The effect of nanoprecipitates on the superelastic properties of FeNiCoAlTa shape memory alloy single crystals, Acta Mater. 61 (2013) 3445–3455.
[25] L.W. Tseng, J. Ma, I. Karaman, S.J. Wang, Y.I. Chumlyakov, Superelastic response of the FeNiCoAlTi single crystals under tension and compression, Scr. Mater. 101 (2015) 1–4.
[26] L.W. Tseng, J. Ma, B.C. Hornbuckle, I. Karaman, G.B. Thompson, Z.P. Luo, Y.I. Chumlyakov, The effect of precipitates on the superelastic response of [1 0 0] oriented FeMnAlNi single crystals under compression, Acta Mater. 97 (2015) 234–244.
[27] A. Walnsch, M.J. Kriegel, M. Motylenko, G. Korpala, U. Prahl, A. Leineweber, Thermodynamics of martensite formation in Fe–Mn–Al–Ni shape memory alloys, Scr. Mater. 192 (2021) 26–31.
[28] M. Vollmer, P. Krooß, M.J. Kriegel, V. Klemm, C. Somsen, H. Ozcan, I. Karaman, A. Weidner, D. Rafaja, H. Biermann, T. Niendorf, Cyclic degradation in bamboo-like Fe–Mn–Al–Ni shape memory alloys-the role of grain orientation, Scr. Mater. 114 (2016) 156–160.
[29] P. Krooß, C. Somsen, T. Niendorf, M. Schaper, I. Karaman, Y. Chumlyakov, G. Eggeler, H.J. Maier, Cyclic degradation mechanisms in aged FeNiCoAlTa shape memory single crystals, Acta Mater. 79 (2014) 126–137.
[30] M. Vollmer, M.J. Kriegel, P. Krooß, S. Martin, V. Klemm, A. Weidner, Y. Chumlyakov, H. Biermann, D. Rafaja, T. Niendorf, Cyclic degradation behavior of <001> -oriented Fe–Mn–Al–Ni single crystals in tension, Shape Mem. Superelasticity 3 (2017) 335–346.
[31] J.A. Simmons, H.N.G. Wadley, Theory of acoustic-emission from phase-transformations, J. Res. Natl. Bur. Stand. 89 (1) (1984) 55–64.
[32] J.E. Kannatey-Asibu, D. Pingsha, Analysis of acoustic emission signal generation during martensitic transformation, J. Manuf. Sci. Eng. 108 (4) (1986) 328–331.
[33] R. Pascual, M. Ahlers, R. Rapacioli, W. Arneodo, Acoustic-emission and martensitic-transformation of beta-brass, Scr. Metall. 9 (1) (1975) 79–84.
[34] K. Ono, T.C. Schlotthauer, T.J. Koppenaal, Acoustic emission from ferrous martensites, J. Acoust. Soc. Am. 55 (2) (1974) 367.
[35] S.M.C. van Bohemen, J. Sietsma, M.J.M. Hermans, I.M. Richardson, Kinetics of the martensitic transformation in low-alloy steel studied by means of acoustic emission, Acta Mater. 51 (14) (2003) 4183–4196.
[36] E. Bonnot, E. Vives, L. Manosa, A. Planes, R. Romero, Acoustic emission and energy dissipation during front propagation in a stress-driven martensitic transition, Phys. Rev. B (Condens. Matter Mater. Phys.) 78 (9) (2008) 094104.
[37] A. Vinogradov, D. Orlov, A. Danyuk, Y. Estrin, Deformation mechanisms underlying tension–compression asymmetry in magnesium alloy ZK60 revealed by acoustic emission monitoring, Mater. Sci. Eng. A 621 (0) (2015) 243–251.
[38] K. Máthis, G. Csiszár, J. Čapek, J. Gubicza, B. Clausen, P. Lukáš, A. Vinogradov, S.R. Agnew, Effect of the loading mode on the evolution of the deformation mechanisms in randomly textured magnesium polycrystals-comparison of experimental and modeling results, Int. J. Plast. 72 (2015) 127–150.
[39] A. Vinogradov, A. Lazarev, M. Linderov, A. Weidner, H. Biermann, Kinetics of deformation processes in high-alloyed cast transformation-induced plasticity/twinning-induced plasticity steels determined by acoustic emission and scanning electron microscopy: influence of austenite stability on deformation mechanisms, Acta Mater. 61 (7) (2013) 2434–2449.
[40] J. Baram, Y. Gefen, M. Rosen, Acoustic-emission generated during a single-interface movement in the martensitic-transformation of Au-47.5-percent Cd alloy, Scr. Metall. 15 (8) (1981) 835–838.
[41] Z. Nishiyama, Martensitic Transformation, Academic Press, New York, 1978 a.o..
[42] Z. Yu, P.C. Clapp, Quantitative analysis of acoustic emission signals, J. Appl. Phys. 62 (6) (1987) 2212–2220.
[43] K. Takashima, Y. Higo, S. Nunomura, The propagation velocity of the martensitic transformation in 304 stainless steel, Philos. Mag. A 49 (2) (1984) 231–241.
[44] M. Vollmer, M.J. Kriegel, A. Walnsch, V. Klemm, A. Leineweber, T. Niendorf, On the microstructural and functional stability of Fe-Mn-Al-Ni at ambient and elevated temperatures, Scr. Mater. 162 (2019) 442–446.
[45] E. Pomponi, A. Vinogradov, A real-time approach to acoustic emission clustering, Mech. Syst. Signal Proc. 40 (2) (2013) 791–804.
[46] A. Vinogradov, D. Orlov, A. Danyuk, Y. Estrin, Effect of grain size on the mechanisms of plastic deformation in wrought Mg–Zn–Zr alloy revealed by acoustic emission measurements, Acta Mater. 61 (6) (2013) 2044–2056.
[47] A. Vinogradov, D. Orlov, A. Danyuk, Y. Estrin, Deformation mechanisms underlying tension–compression asymmetry in magnesium alloy ZK60 revealed by acoustic emission monitoring, Mater. Sci. Eng. A 621 (2015) 243–251.
[48] C.B. Scruby, H.N.G. Wadley, J.J. Hill, Dynamic elastic displacements at the surface of an elastic half-space due to defect sources, J. Phys. D Appl. Phys. 16 (6) (1983) 1069–1083.
[49] S. Kullback, R.A. Leibler, On information and sufficiency, Ann. Math. Stat. 22 (1) (1951) 79–86.
[50] R. Sidharth, Y. Wu, F. Brenne, W. Abuzaid, H. Sehitoglu, Relationship between functional fatigue and structural fatigue of iron-based shape memory alloy FeMnNiAl, Shape Mem. Superelasticity 6 (2020) 256–272.
[51] L.W. Tseng, Ji. Ma, S.J. Wang, I. Karaman, M. Kaya, Z.P. Luo, Y.I. Chumlyakov, Superelastic response of a single crystalline FeMnAlNi shape memory alloy under tension and compression, Acta Mater. 89 (2015) 374–383.
[52] Y. Liu, I. Houver, H. Xiang, L. Bataillard, S. Miyazaki, Strain dependence of pseudoelastic hysteresis of NiTi, Metall. Mater. Trans. 30A (1999) 1275–1283.
[53] A. Vinogradov, M. Nadtochiy, S. Hashimoto, S. Miura, Correlation between spectral parameters of acoustic-emission during plastic-deformation of Cu and Cu-Al single and polycrystals, Mater. Trans. JIM 36 (3) (1995) 426–431.
[54] A. Vinogradov, A. Lazarev, Continuous acoustic emission during intermittent plastic flow in α-brass, Scr. Mater. 66 (10) (2012) 745–748.
[55] A. Vinogradov, I.S. Yasnikov, Y. Estrin, Stochastic dislocation kinetics and fractal structures in deforming metals probed by acoustic emission and surface topography measurements, J. Appl. Phys. 115 (23) (2014) 233506.
[56] A. Ojha, H. Sehitoglu, Transformation stress modeling in new FeMnAlNi shape memory alloy, Int. J. Plast. 86 (2016) 93–111.
[57] G.B. Olson, M. Cohen, A general mechanism of martensitic nucleation- Part II. FCC $\rightarrow$ BCC and other martensitic transformations, Metall. Trans.A 7 (1976) 1905.
[58] J.M. Vallejos, C.E. Sobrero, M. Avalos, J.W. Signorellia, J.A. Malarria, Crystallographic orientation relationships in the $\alpha \rightarrow \gamma'$ martensitic transformation in an Fe–Mn–Al–Ni system, J. Appl.Crystallogr. 51 (2018) 990–997.
[59] P.D.B. Fischer, S. Martin, A. Walnsch, M. Thümmler, M.J. Kriegel, A. Leineweber, Nanoscale twinning in Fe–Mn–Al–Ni martensite: a backscatter Kikuchi diffraction study, J. Appl. Crystallogr. 54 (2021) 54–61.
[60] L.W. Tseng, Ji. Ma, S.J. Wang, I. Karaman, Y.I. Chumlyakov, Effects of crystallographic orientation on the superelastic response of FeMnAlNi single crystals, Scr. Mater. 116 (2016) 147–151.
[61] L.W. Tseng, J. Ma, Y.I. Chumlyakov, I. Karaman, Orientation dependence of superelasticity in FeMnAlNi single crystals under compression, Scr. Mater. 166 (2019) 48–52.
[62] T. Maki, C.M. Wayman, Effect of coherent precipitates in austenite on the martensite substructure in an Fe-Ni-Ti-C alloy, Acta Metall. 25 (1977) 695–710.
[63] T. Omori, M. Nagasako, M. Okano, K. Endo, R. Kainuma, Microstructure and

martensitic transformation in the Fe-Mn-Al-Ni shape memory alloy with B2-type coherent fine particles, Appl. Phys. Lett. 101 (2012) 231907.
[64] A. Walnsch, M.J. Kriegel, P.D.B. Fischer, S. Neumann, D. Rafaja, A. Leineweber, Nanoscale twinning and superstructures of martensite in the Fe–Mn–Al–Ni system, Materialia 16 (2021) 101062.
[65] M. Vollmer, C. Segel, P. Krooß, J. Günther, L.W. Tseng, I. Karaman, et al., On the effect of gamma phase formation on the pseudoelastic performance of polycrystalline Fe–Mn–Al–Ni shape memory alloys, Scr. Mater. 108 (2015) 23–26.
[66] M. Vollmer, T. Arold, M.J. Kriegel, V. Klemm, S. Degener, J. Freudenberger, T. Niendorf, Promoting abnormal grain growth in Fe-based shape memory alloys through compositional adjustments, Nat. Commun. 10 (2019) 2337.
[67] T. Birk, S. Biswas, J. Frenzel, G. Eggeler, Twinning-induced elasticity in NiTi shape memory alloys, Shape Mem. Superelasticity 2 (2016) 145–159.
[68] Y.F. Zheng, B.M. Huang, J.X. Zhang, L.C. Zhao, The microstructure and linear superelasticity of cold-drawn TiNi alloy, Mater. Sci. Eng. A 279 (1–2) (2000) 25–35.
[69] L.C. Zhao, Y.F. Zheng, W. Cai, Study of deformation micromechanism in cold-deformed TiNi based alloys, Intermetallics 13 (3–4) (2005) 281–288.
[70] E. Hornbogen, On the term pseudo-elasticity, Z. Metallkd. 86 (5) (1995) 341–344.
[71] A. Planes, E. Vives, Avalanche criticality in thermal-driven martensitic transitions: the asymmetry of the forward and reverse transitions in shape-memory materials, J. Phys. Condens. Matter 29 (33) (2017) 334001.
[72] D.L. Beke, M.K. Bolgár, L.Z. Tóth, L. Daróczi, On the asymmetry of the forward and reverse martensitic transformations in shape memory alloys, J. Alloys Compd. 741 (2018) 106–115.
[73] K. Yoshida, S. Kihara, K. Sakamaki, Evaluation of martensitic transformation dynamics of Cu-Al-Ni shape memory alloy single crystal by acoustic emission method, J. Acoust. Emiss. 18 (2000) 68–74.
[74] A. Planes, D. Rouby, J.L. Macqueron, M. Morin, G. Guenin, Energetic measurements of the acoustic-emission generated during the martensitic-transformation of a Cu-Zn-Al alloy, J. Phys. D Appl. Phys. 15 (1) (1982) 89–95.
[75] A. Planes, J.L. Macqueron, M. Morin, G. Guenin, Study of martensitic-transformation of Cu-Zn-Al alloy by coupled enthalpy and acoustic-emission measurements, Phys. Status Solidi A Appl. Res. 66 (2) (1981) 717–724.
[76] J. Baram, M. Rosen, On the nature of the thermoelastic martensitic phase–transformation in Au 47.5 at percent Cd determined by acoustic-emission, Acta Metall. 30 (3) (1982) 655–662.
[77] J.K. Lee, H.C. Kim, Acoustic-emission during martensitic-transformation of a Cu-Mn-Al alloy, J. Mater. Sci. Lett. 7 (7) (1988) 722–724.
[78] L.I. Manosa, A. Planes, E. Cesari, Acoustic-emission amplitude dstribution during the martensitic-transformation of Cu-Zn-Al alloys, J. Phys. D Appl. Phys. 22 (7) (1989) 977–982.
[79] A. Planes, L. Mañosa, E. Vives, Acoustic emission in martensitic transformations, J. Alloys Compd. 577 (2013) S699–S704.
[80] L. Straka, V. Novák, M. Landa, O. Heczko, Acoustic emission of Ni-Mn-Ga magnetic shape memory alloy in different straining modes, Mater. Sci. Eng. A 374 (1–2) (2004) 263–269.
[81] P. Sittner, Y. Liu, V. Novak, On the origin of Lüders-like deformation of NiTi shape memory alloys, J. Mech. Phys. Solids 53 (2005) 1719–1746.
[82] L. Zheng, Y. He, Z. Moumni, Effects of Lüders-like bands on NiTi fatigue behaviors, Int. J. Solids Struct. 83 (2016) 28–44 April.